WITS
UNIVERSITY

A study of the dopant effect in metal pyrophosphates and their potential for use in supercapacitors.

Andrew van der Riet

Supervised by

Dr Roy P. Forbes

Declaration

I declare that this dissertation is my own, unaided work. It is being submitted for the Degree of Master of Science at the University of the Witwatersrand, Johannesburg. It has not been submitted before for any degree or examination at any other University.

(Signature of candidate)

5th day of September 2024 at University of the Witwatersrand

Abstract

This dissertation focuses on the comprehensive characterization of two sample sets of $La_xHf_{1-x}P_2O_7$, denoted as Group 1 and 2, synthesised through two variations of the sol-gel method, shedding light on their structural and functional characteristics. Employing a range of characterisation techniques such as Powder X-ray Diffraction (PXRD), ^{31}P Magic Angle Spinning Solid-State Nuclear Magnetic Resonance (^{31}P MAS ssNMR) spectroscopy, Pair Distribution Function (PDF), Fourier Transform Infrared (FTIR) Spectroscopy, Transmission Electron Microscopy (TEM), Simultaneous Thermal Analysis (STA), and Potentiometric Electrochemical Impedance Spectroscopy (PEIS), this study achieved a thorough understanding of the materials' composition, structure, and physical properties.

The PXRD analysis suggested that the materials from Group 1 were amorphous, contrasting with the crystalline behaviour of Group 2's materials. A pre-existing structure model of HfP_2O_7 was fitted to Group 2's PXRD data using the Rietveld refinement method with satisfactory fits, confirming the composition and structure of the materials, as well as emphasizing their crystalline nature. The ^{31}P MAS ssNMR analysis revealed distinct phosphorous signals for both groups, elucidating their differing phosphorous environments.

PDF data provided insights into short-range order for Group 1 and refined structural models for Group 2, enabling qualitative comparisons between the two groups. FTIR spectra confirmed the presence of pyrophosphate functional groups in both groups. TEM images substantiated the amorphous and crystalline nature of Group 1 and Group 2 materials, respectively, with dominant particle sizes in the 20-30 nm range.

STA data highlighted excellent thermal stability in both groups, crucial for high-temperature applications. PEIS data indicated enhanced ionic conductivity upon La^{3+} doping, albeit lacking a clear trend with varying dopant concentrations.

Additionally, distinct synthetic procedures for Group 1 and Group 2 resulted in materials with different morphologies. Group 1's method led to amorphous materials, attributed to solvent elimination before calcination, while Group 2's approach yielded crystalline materials due to evaporation in air before calcination.

These findings underscore the impact of subtle synthetic variations on material properties, emphasizing the need for precise control in synthesis parameters. Overall, this research provides valuable insights into $La_xHf_{1-x}P_2O_7$ materials for energy applications, paving the way for further advancements in metal pyrophosphates and materials science as a whole.

Dedication

I would like to dedicate this dissertation to all the people in my life that supported me on this journey.

Acknowledgements

I would like to express my sincere gratitude to the following individuals for their invaluable contributions to this dissertation:

Dr. Memory Zimuwandeyi's assistance with ^{31}P MAS ssNMR data collection, and Tracy Lau's guidance and training on the FTIR instrument was greatly appreciated and contributed significantly to the experimental outcomes of this research. Darren Fynn's assistance in training me on the STA instrument was crucial for obtaining quality thermal data. The Wits MMU team provided essential instrument training for TEM, and I am grateful to Prof. Alexander Ziegler for his assistance in capturing images of three samples. I am also grateful to Jacques Gerber's expertise in pellet coating at Wits MMU which was essential for PEIS sample preparation, and I extend my thanks to Prof. Caren Billing for her training on the PEIS instrument.

My supervisor, Dr. Roy P. Forbes who provided comprehensive training on the D8 Advance and D2 diffractometers and imparted expertise in utilizing TOPAS 5 for data analysis. A special thanks for his dedication to my research, which included flying out to the ESRF in France to collect PDF data, which significantly enhanced the quality and outcome of this dissertation.

Their expertise, guidance, and support were instrumental in the successful completion of this dissertation.

Table of Contents

List of figures

List of tables

List of Acronyms & Abbreviations

AMP: Adenosine Monophosphate

ATP: Adenosine Triphosphate

AXS: Advanced X-ray Solutions

CCD: Charge Coupled Device

CIF: Crystallographic Information File

COD: Crystallography Open Database

CPE: Constant Phase Element

DTA: Differential Thermal Analysis

EC: ElectroChemistry [Lab]

EDLC: Electrochemical Double Layer Capacitor

EDS: Energy Dispersive X-ray Spectroscopy

EIS: Electrochemical Impedance Spectroscopy

ESRF: European Synchrotron Radiation Facility

FEI: Field Electron and Ion [Company]

FTIR: Fourier Transform Infrared [Spectroscopy]

GUI: Graphical User Interface

HR-TEM: High Resolution Transmission Electron Microscopy/Microscope

HT: High Temperature

ICSD: Inorganic Crystal Structure Database

LIB: Lithium-Ion Battery

LT: Low Temperature

MAS: Magic Angle Spinning

MMU: Microscopy and Microanalysis Unit

NMR: Nuclear Magnetic Resonance

OCP: Open Circuit Potential

OPUS: Optical User Software

PDF: Pair Distribution Function

PEIS: Potentiometric Electrochemical Impedance Spectroscopy

PEMFC: Proton Exchange Membrane Fuel Cell

PSC: Pseudo-Supercapacitor

PVA: Polyvinyl Alcohol

PXRD: Powder X-Ray Diffraction

SEM: Scanning Electron Microscopy/Microscope

STA: Simultaneous Thermal Analyser/Analysis

TEM: Transmission Electron Microscope/Microscopy

TGA: Thermal Gravimetric Analysis

TOPAS: Total Pattern Analysis Solution

UV: Ultraviolet

VESTA: Visualisation for Electronic Structural Analysis

VMP: Versatile Multichannel Potentiostat

Chapter 1: Introduction

1.1 Preface

The increasing energy needs of a growing global population is accelerating climate change and causing other environmental problems. Accordingly, there has been an increasing amount of effort focusing on finding solutions to these challenges. Commensurately, there has been an increase drive to move towards environmentally friendly and sustainable energy storage and energy conversion devices. These include extensive research efforts in the development of supercapacitors, fuel cells, and solid-state batteries all of which have been of great interest in recent years [1].

1.2 Ceramics

Advanced ceramics are crystalline materials of inorganic nature, distinguished by their strictly controlled composition and microstructure [2]. Advanced ceramics offer properties such as high thermal stability, low density, wear resistance, and promising conductive properties, which are highly desirable in energy devices [3]. A few examples of advanced ceramic materials include metal oxides such as zirconia (ZrO_2) [4] and alumina (Al_2O_3) [5], silicon nitride (Si_3N_4) [6], and metal pyrophosphates such as zirconium pyrophosphate (ZrP_2O_7) [7], titanium pyrophosphate (TiP_2O_7) [8], and sodium acid pyrophosphate ($Na_2H_2P_2O_7$) [9], to name a few. Pyrophosphates have shown the potential for many applications, including catalysis, materials science, and materials engineering [10].

1.3 Overview of Pyrophosphates

Ceramics that contain the pyrophosphate ion ($P_2O_7^{4-}$) have been studied extensively due to their physical properties. These properties include high thermal stability up to 400 °C as previously recorded [11] and high ionic conductivities, from 10^{-6} – 10^{-1} S.cm^{-1} in a humidified atmosphere in 100 – 300 °C range [12].

Due to its structure and chemical stability, $P_2O_7^{4-}$ features in several different classes of compounds. $P_2O_7^{4-}$ is comprised of two phosphate groups bound together by an oxygen atom, forming a P–O–P link [13]. They can be produced via the hydrolysis of phosphoric acid [14] or biologically by hydrolysing adenosine triphosphate (ATP) into adenosine monophosphate (AMP) [15]. These compounds play a vital role in the world of biochemistry and molecular biology, participating in a broad array of biochemical reactions. Beyond biological applications, materials that contain the pyrophosphate anion have been reported to have extensive uses across various scientific and engineering domains. For example, $P_2O_7^{4-}$ containing materials play an essential role in dental care products, where they prevent plaque formation [16], and in the food industry, pyrophosphates serve as preservatives, emulsifiers, and leavening agents [17], [18]. Their effectiveness in controlling water hardness and preventing scaling has also made them essential water treatment agents [19]. A large class of pyrophosphates known as metal pyrophosphates have also been studied extensively. Owing to their structure, metal pyrophosphates show potential for the use as ionic conductors [1].

1.4 Metal Pyrophosphates

Metal Pyrophosphates have the general formulae of $M^{IV}P_2O_7$, $M^{II}_2P_2O_7$, $M^{I}M^{III}P_2O_7$, $M^{I}_2M^{II}P_2O_7$ and $M^{I}_4P_2O_7$ [20]. A few examples of pyrophosphates include nickel pyrophosphate ($Ni_2P_2O_7$), nickel cobalt pyrophosphate ($NiCoP_2O_7$), titanium pyrophosphate (TiP_2O_7), which adopts two polymorphs, a low temperature (LT-TiP_2O_7) phase and high temperature (HT-TiP_2O_7) titanium pyrophosphate phase [20]. More examples are listed in Table 1.1.

$Ni_2P_2O_7$ and TiP_2O_7 have been studied for their unique properties and applications in various fields. $Ni_2P_2O_7$ was investigated for its electrocatalytic activity [21] and morphology variations [22], which are crucial for applications in supercapacitors and electrochemical energy storage. On the other hand, titanium pyrophosphate has garnered attention due to its exceptional proton conductivity properties [23], making it a promising material for proton conductors and electrolytes in fuel

cells. These studies therefore aimed to explore their potential in enhancing energy storage technologies and advancing proton conductivity applications.

Table 1.1: Examples of several pyrophosphates listed alongside their structural parameters.

MP_2O_7	Crystal System	Unit cell parameters (Å)			β (°)	Space Group
		a	b	c		
$NiH_2P_2O_7$ [24]	Monoclinic	9.09600	12.59300	9.59990	106.47	$P2_1/c$
TiP_2O_7 [25]	Cubic	7.88042	7.88042	7.88042	90	$Pa\bar{3}$
ZrP_2O_7 [26]	Cubic	8.24740	8.24740	8.24740	90	$Pa\bar{3}$
SnP_2O_7 [27]	Cubic	8.25000	8.25000	8.25000	90	$Pa\bar{3}$
HfP_2O_7 [28]	Orthorhombic	24.652	24.6296	24.651	90	*Pbca*
HfP_2O_7 [29]	Cubic				90	$Pa\bar{3}$

Tetravalent metal pyrophosphates ($M^{IV}P_2O_7$,) tend to crystallize with cubic symmetry while metal acid pyrophosphates such as $NiH_2P_2O_7$ crystallize with monoclinic crystal symmetry [24]. With respect to the tetravalent metal pyrophosphates, the structure is comprised of corner shared oxygen atoms that form phosphate tetrahedra and metal octahedra (Figure 1.1).

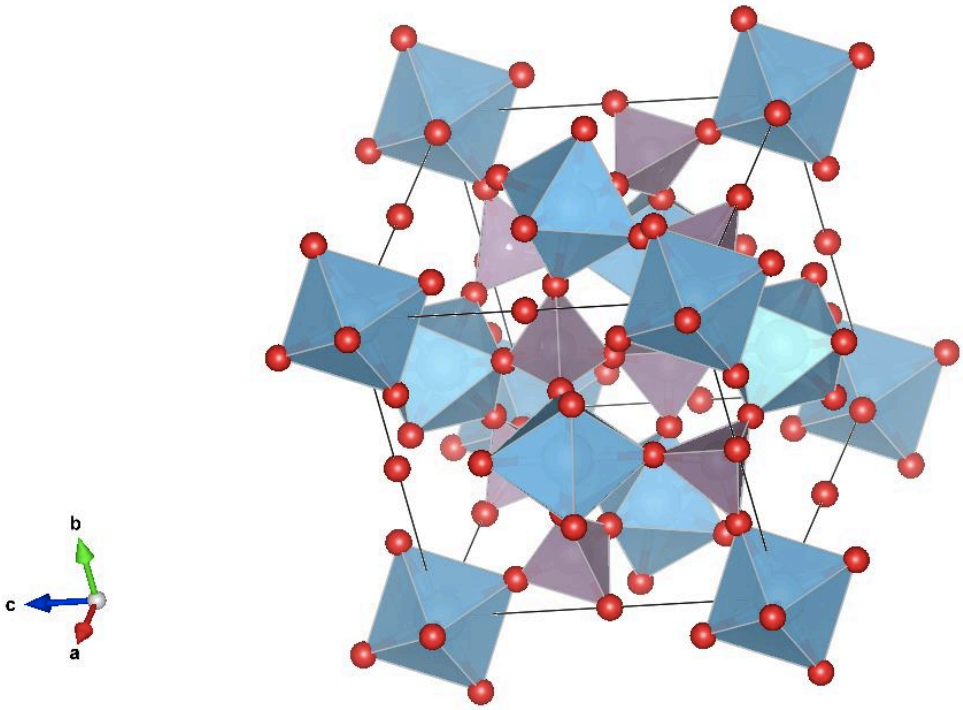

Figure 1.1: Unit cell crystal structure of TiP_2O_7 (Ti = blue, P = lilac, O = red, Ti tetrahedra = blue) (CIF file from [30] was opened and captured using the VESTA program)

Metal pyrophosphates exhibit diverse framework architectures, largely influenced by the metal ions involved and the conditions under which they are synthesised. These frameworks can be classified into several types: layered, chain, 3D, and mixed anion structures. Layered structures are characterised by two-dimensional sheets of metal ions connected by pyrophosphate groups, which is observed in compounds such as zinc or iron pyrophosphates [31]. Chain structures consist of one-dimensional chains where metal cations are linked by pyrophosphate groups, typical in calcium or strontium pyrophosphates. Three-dimensional frameworks are fully interconnected networks that may exhibit porosity, as seen in certain zeolite-like structures [32]. Additionally, mixed anion structures incorporate other anions, such as hydroxides, adding complexity to the overall framework.

These frameworks can also be classified based on the geometry of the metal centres. Tetrahedral frameworks involve metal centres in a tetrahedral arrangement, where the pyrophosphate groups bridge the metal ions [33]. Octahedral frameworks feature metal centres in an octahedral coordination,

connected through pyrophosphate units [34]. Chain-like frameworks describe linear or zigzag chains of metal ions connected by pyrophosphate units, while layered frameworks involve stacked layers of metal ions and pyrophosphate groups held together by weak interactions [35]. These various structures are crucial for applications in catalysis and the development of functional materials [33].

These pyrophosphates have been found to exhibit desirable physical properties; TiP_2O_7 has shown to exhibit active redox behaviour [36], ZrP_2O_7 exhibits high thermal and chemical stability and has also been shown proton conductivity [37]. SnP_2O_7 has been studied for its use as a catalyst in organic synthesis [38]. HfP_2O_7 has been studied for its UV luminescence properties [39].

1.5 The Role of Dopants in Metal Pyrophosphates

The addition of dopants to metal pyrophosphates have been shown to improve its electrochemical [10], thermal [40], and optical [15] properties [41]. Doping has been widely used in semi-conductor materials [42], [43], [44], [45]. The purpose of doping is to introduce a small quantity of a foreign substance to an existing material [46] in the hopes of altering its chemical and physical properties [45]. For semi-conducting materials, the dopant element is often similar in size to the element being displaced but contains either more or less electrons (Figure 1.2) [47]. This introduces the potential for an increase in charge carriers or holes in the material (Figure 1.2), which could potentially improve its ionic conductivity [48].

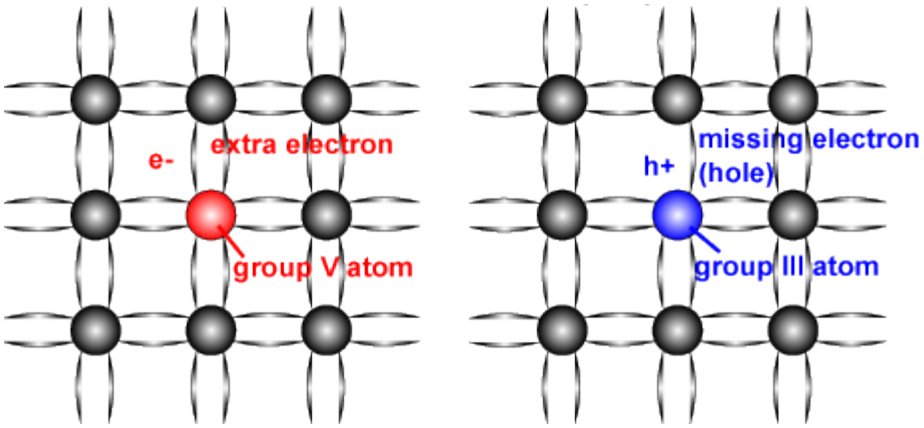

Figure 1.2: Example of a material that was first doped with a dopant carrying one more electron than the original element, and the second with a dopant carrying one less electron than the original element [47].

Metal pyrophosphates have been doped with cations of reduced valency to potentially improve their ionic conductivity by increasing the number of electron holes making more sites available for proton 'hopping' [49], [50] – (Figure 1.3)

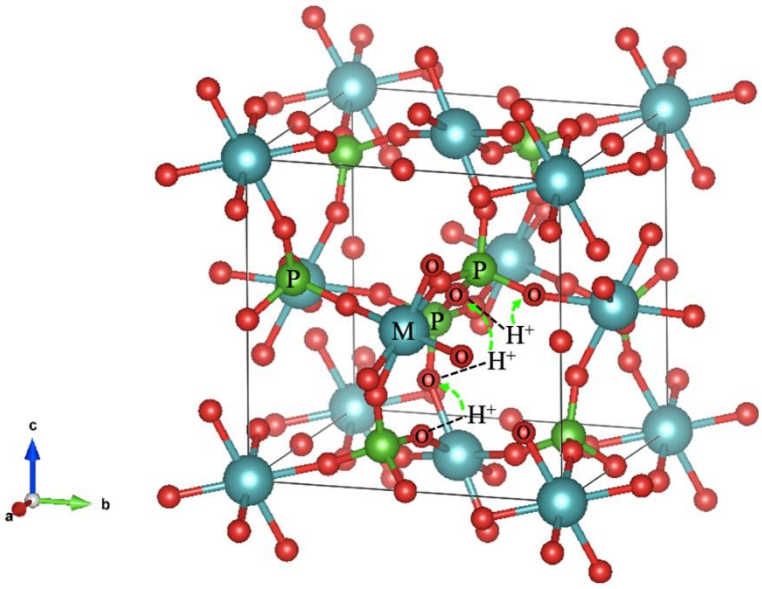

Figure 1.3: Unit cell of a cubic metal pyrophosphate (space group: $Pa\bar{3}$) demonstrating the proton 'hopping' mechanism – produced in VESTA, adapted from [44].

While proton conduction can occur in metal pyrophosphates, this is not the only mechanism by which ionic conduction occurs in metal pyrophosphates. Ionic conduction, briefly mentioned earlier, can occur via the migration of metal ions through the material, which is facilitated by the electrostatic forces present in the material [51]. The electrostatic forces allow for the movement of the metal ions

through the lattice, giving rise to cationic vacancy defects that result in additional movement of metal ions through the lattice [51]. This movement of metal ions, and therefore charge, results in a net ionic flow of ions which results in a net ionic conductivity.

Overall, this study showed no improvement of proton conductivity was achieved by this method of doping, however, ionic conductivity did improve overall due to the introduction of interstitial defects from the addition of lower valence cationic dopants.

1.6 Synthesis and Characterisation of Doped and Undoped Metal Pyrophosphates

Numerous synthetic methods have been explored in the synthesis of metal pyrophosphates, including microwave-assisted solid-state method [52], sol-gel method [53], [54], and the co-precipitation method [55], [56]. The next section contains a brief description of these synthesis methods as they are applied to metal pyrophosphates based on an analysis of published literature.

Microwave-assisted solid-state method

The microwave-assisted solid-state method was used for the synthesis of $Pb_2P_2O_7$. This synthetic route is highly desirable due to its quick synthesis time of just 10 minutes [52], compared to, for example, the sol-gel method which often requires many hours of calcination time in the furnace, as stated under the Sol-gel method section ahead. Microwave-assisted synthesis works by penetrating the material, generating heat directly through material-microwave interaction. This interaction involves excitation of microwave electromagnetic radiation aligning the dipoles of a material in an external field. This causes direct heating of the material and is therefore a much faster heating process than conventional heating [57].

Sol-gel method

The sol-gel method (Figure 2.1) is a widely used synthetic method for the synthesis of ceramics [58], [59], [60], and numerous metal pyrophosphates have been synthesized by this method [53], [54]. The sol-gel process is a chemical reaction

that transforms a system from "sol" – a dispersion of colloidal particles in a liquid – into a gelatinous network called the "gel". The gel is then calcined and annealed to get rid of any organic matter, as well as advance the chemical reaction to completion [61]. Windarti et al., 2017 showed that the synthesis of β-$Ca_2P_2O_7$ is possible via the sol-gel method with a total reaction time of 21 hours (8 hours dedicated to calcination) [53]. This study showed a comprehensive overview of how increasing the calcination temperature increased the degree of crystallinity of the material.

Co-precipitation method

Co-precipitation is the simultaneous precipitation of two or more compounds from a solution, followed by solvent removal and calcination. It has also proven to be a convenient method for the preparation of metal pyrophosphates [36]. Both Senthilkumar et al. 2015 [62] used the co-precipitation in their studies to synthesise metal pyrophosphates. Senthilkumar et al. 2015 [62] investigated how the co-precipitation method can yield $Ni_2P_2O_7$ and Griesiute et al., 2022 [55] showed how this method can yield α-, β-, and γ- phases of $Ca_2P_2O_7$.

1.7 The Application of Metal Pyrophosphates in Energy Devices

An important application of pyrophosphates, more specifically metal pyrophosphates, would be their use in energy storage and sensor devices [63]. The application of pyrophosphates has shown promise for use in supercapacitors [64] as they display comparably good ionic conductivity and excellent redox behaviour to existing materials used in supercapacitors [40].

In addition to the electrochemical properties, metal pyrophosphates have also been shown to possess unusual thermal properties. It was discovered that below a temperature of 293 °C, ZrP_2O_7 exhibited the expected positive thermal expansion. However, above this temperature, negative thermal expansion occurred [20], i.e. the material contracts with increasing temperature as opposed to the positive thermal expansion commonly observed in solids such as metals (e.g. aluminium).

Modelling suggested that the negative thermal expansion occurred as a result of the bending of $P_2O_7^{4-}$ units away from the ideal angle of 180 ° (Figure 1.4), leading to a reduction in the overall cell volume [20]. The combination of these physical properties could prove to be potentially beneficial. For example, while most supercapacitors are operated at or below 200 °C [65], the high temperature structural stability of the pyrophosphates could potentially be exploited to access ionic conductivity at elevated temperatures. Therefore, the applications of metal pyrophosphates in energy devices play a significant role in enhancing the efficiency and longevity of various components, thus contributing to the overall advancement of energy devices.

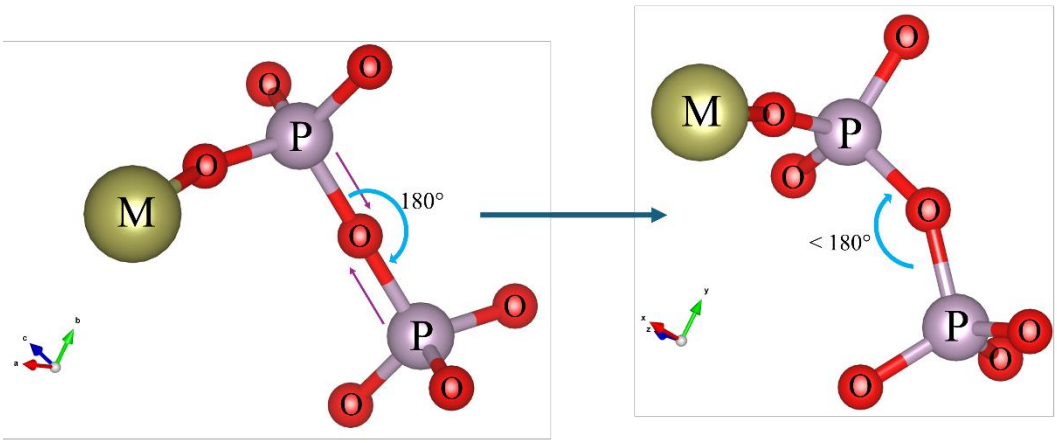

Figure 1.4: Example of pyrophosphate bridge (P–O–P) bending away from the ideal angle of 180 ° due to negative thermal expansion.

1.8 Energy Devices

Supercapacitors

Supercapacitors are electrochemical energy storage devices [66] that consist of two permeable electrodes that are placed in an electrolytic medium where ions flow from the electrolyte to the porous membrane of the electrodes [67]. Supercapacitors can be categorised into double layer capacitors, hybrid supercapacitors and pseudo-supercapacitors (Figure 1.5).

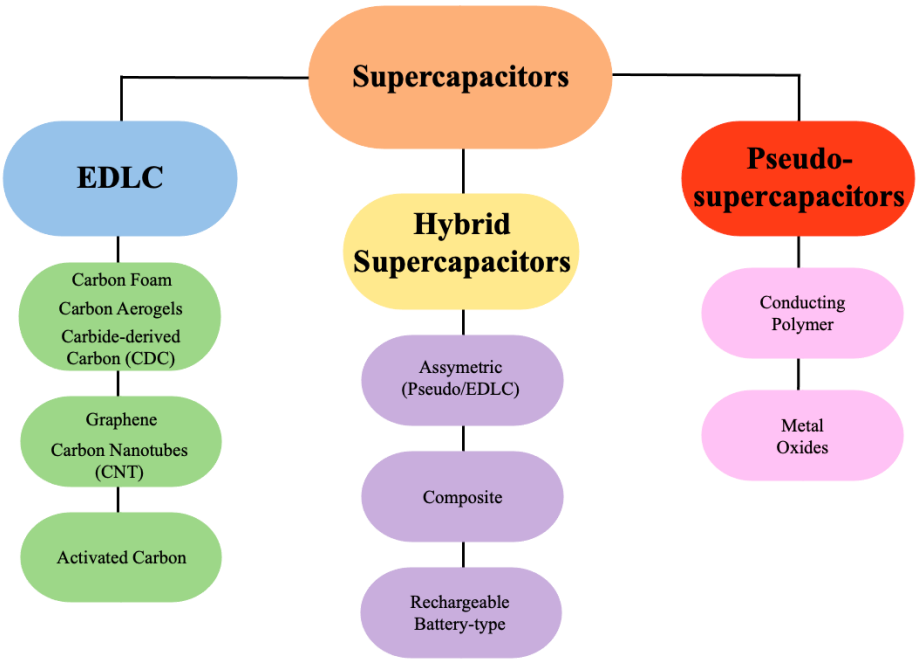

Figure 1.5: Brief overview of the different supercapacitors and their characteristics [68].

EDLC's are supercapacitors that can be identified by their large surface area electrodes (nano-structured and nano-porous materials), their large capacitance and the presence of an electrolyte [69]. The EDLC stores energy electrostatically by forming a 'double layer' of ions at the surface of each electrode creating a double layer capacitance (Figure 1.6).

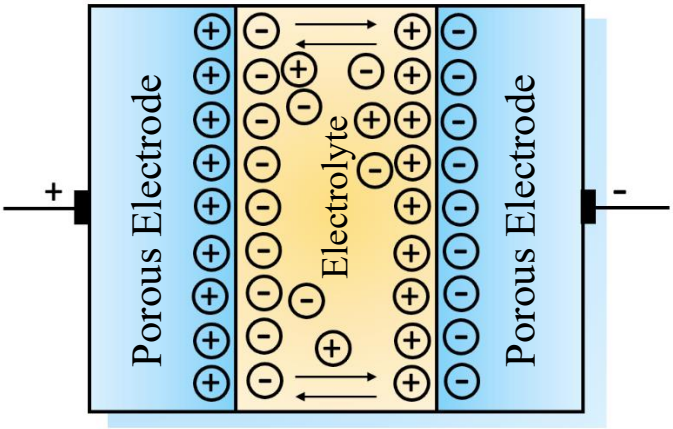

Figure 1.6: Diagram of an EDLC, showing the storage of ions (+ and –) in a "double layer" and their movement across the electrolyte while operating.

Pseudo-supercapacitors (Figure 1.7), are devices whose electrodes are comprised of redox active materials, which store charge through a different mechanism compared to EDLCs [70], which store electrostatic charge. They store energy via

fast, reversible faradic redox reactions that occur at or near the surface of the electrodes [71]. The electrochemical charge transfer creates pseudo-capacitance that stores the energy [72]. Metal oxides, metal nitrides, metal hydroxides, metal sulphides, and conducting polymers are common pseudocapacitive materials [73].

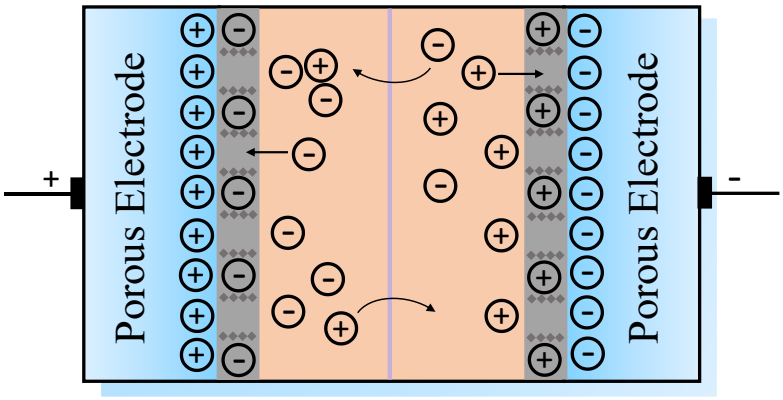

Figure 1.7: Diagram of a pseudo-supercapacitor illustrating the intercalation of ions within their respective electrode materials.

The last category of supercapacitors is that of hybrid supercapacitors (Figure 1.8) which have been intended to integrate the benefits of both EDLCs and pseudo-supercapacitors into one system to achieve a balance between high power and energy density [74]. This was done by merging electrochemical storage of charge found in, for example, a lithium-ion battery (LIB) and electrostatic storage of charge.

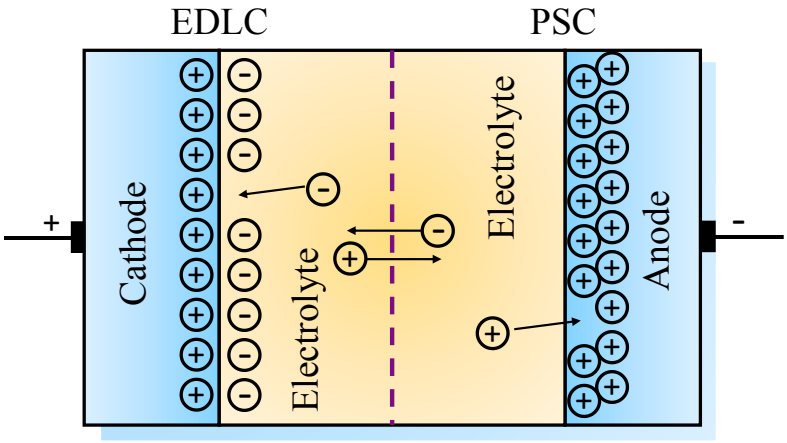

Figure 1.8: Diagram of an EDLC/Pseudo-Supercapacitor (PSC) hybrid supercapacitor, wherein the cathodic side of the cell mimics that of an EDLC, and the anodic side of the cell mimics that of a PSC.

These hybrid systems often use a combination of carbon-based materials (EDLC-like behaviour) and conducting polymers or transition metal oxides (pseudo-capacitive behaviour) to enhance performance, with specific improvement in energy density [75]. Figure 1.9 depicts a comparison of power and energy density of different energy devices; it shows that supercapacitors have a broad range of both power density and energy density, which provides potential to develop and improve upon these supercapacitors.

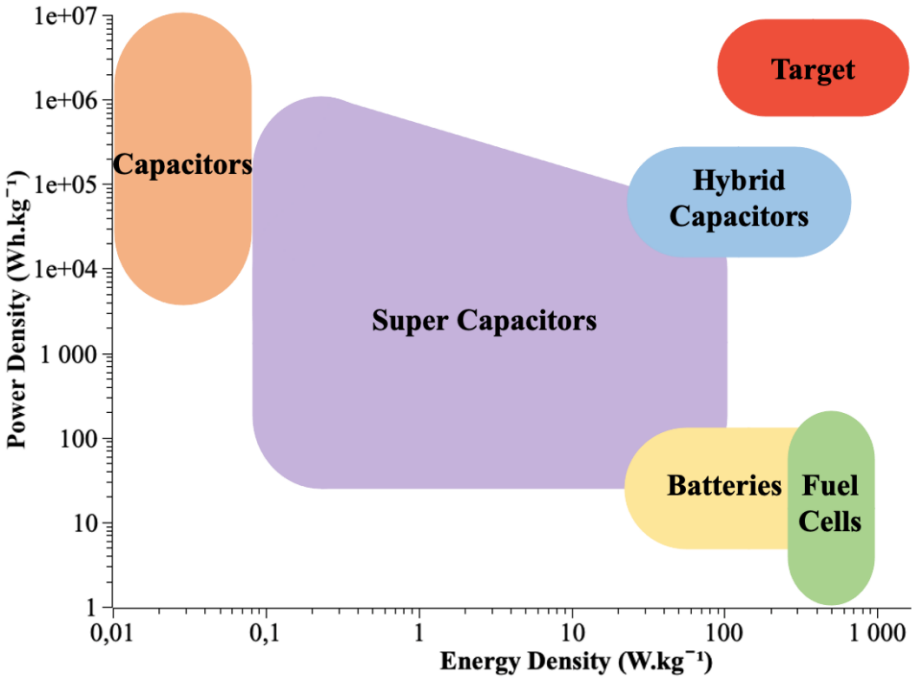

Figure 1.9: Comparison of power and energy densities in different energy storage and conversion devices.

Several materials have been investigated for use as supercapacitor electrolytic materials. A few include, LiCl – dry solid polymer electrolyte [76], PVA – gel polymer electrolyte [77], and Li_2S-P_2S_5 – inorganic electrolyte [78]. Liquid electrolytes usually comprise of lithium salts dissolved in ionic liquids [79]. These, however, can pose problems since liquid electrolytes are volatile and flammable, which is not desirable in devices that may operate at raised temperatures. Solid-state electrolytes may, therefore, be more durable in these conditions.

Fuel Cells

Fuel cells are electrochemical devices that convert chemical energy ('fuel') into electrical energy via a chemical reaction [80]. They operate based on the principle of electrochemical reactions involving fuel and oxidizing agents, by way of redox reactions. The most common type of fuel cell is the proton exchange membrane fuel cell (PEMFC), which is widely used in various applications, including transportation and stationary power generation [81]. Fuel cells work by oxidising hydrogen gas (the fuel) at the anode, releasing electrons and protons. The electrons then travel through the anode to the electrical load providing it with energy. The

electrons then travel down the cathode, reacting with oxygen from the air, and the protons travel through the electrolyte/membrane from the anode to the cathode and produce water. This reaction is illustrated in Figure 1.10.

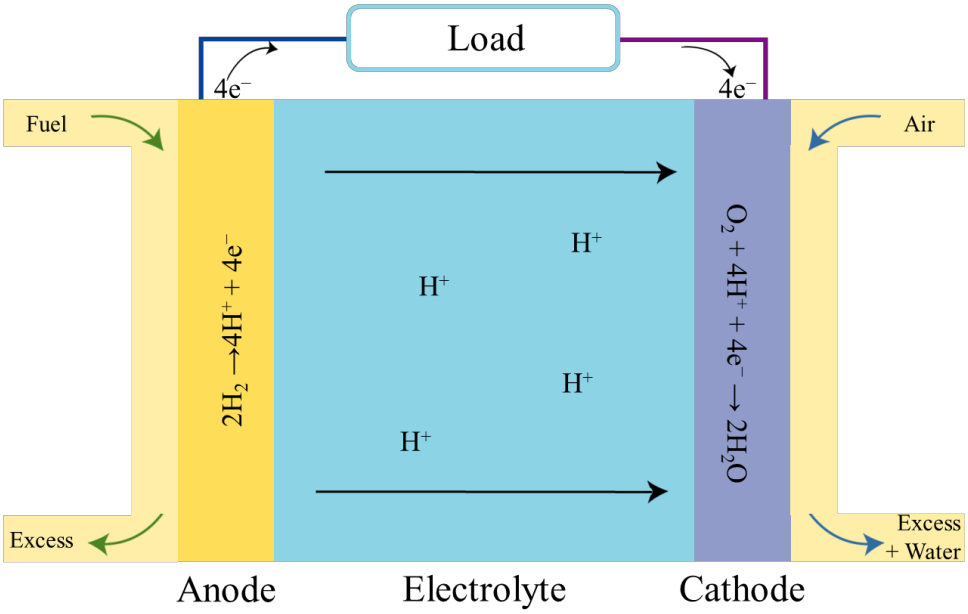

Figure 1.10: Diagram of a fuel cell describing the reactions involved in the conversion of chemical energy (fuel) into electrical energy and the flow of charge through the device [82].

Different fuel cells exist and include Proton Exchange Membrane Fuel Cells (PEMFCs), Alkaline Fuel Cells (AFCs), Solid Oxide Fuel Cells (SOFCs), and Phosphoric Acid Fuel Cells (PAFCs) which all use hydrogen as their fuel, and Molten Carbonate Fuel Cells (MCFCs), and Direct Methanol Fuel Cells (DMFCs) [83]. While hydrogen is the main source of energy, pure hydrogen is not always available and therefore different sources of hydrogen could be used. These fuels include methanol, used in DMFCs and hydrocarbons, in addition to hydrogen, in MCFCs. While these give rise to more fuel options, they also yield CO_2 as a byproduct which defeats the purpose of green energy [83]. Figure 1.11 illustrates how different fuel cells work, all using the same or a similar concept to that illustrated in Figure 1.10.

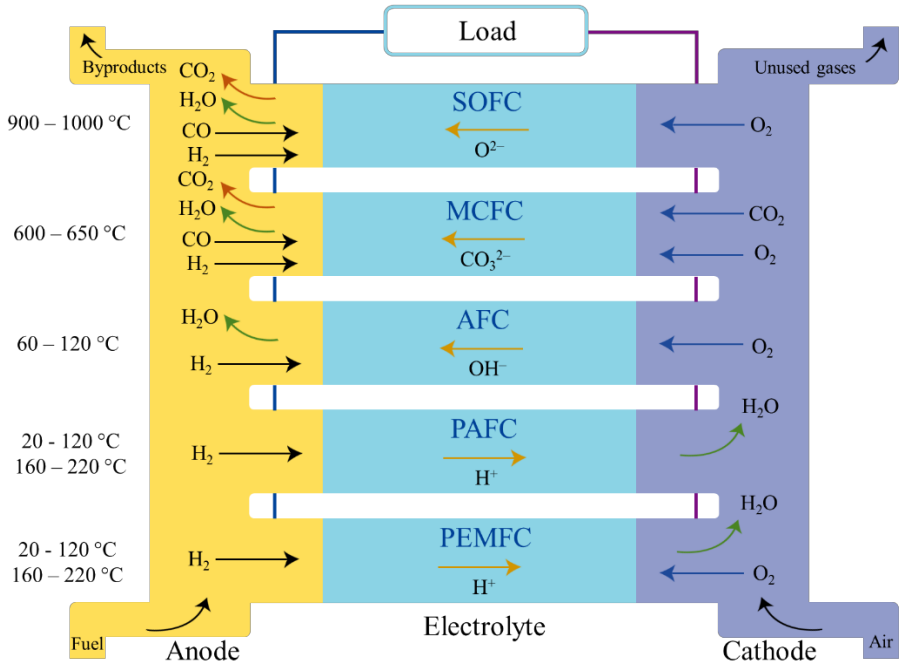

Figure 1.11: Diagram of how different fuel cells run to generate electrical energy [84].

While fuel cells are an incredible leap forward in technology, a huge concern with most fuel cells is their use of hydrogen as their fuel in conjunction with their operating temperatures. As illustrated in Figure 1.11, the operating temperature, depending on the fuel cell, ranges between 20 °C to 1000 °C, which is dangerous since hydrogen, when mixed with air in certain conditions, for example, elevated temperatures, forms explosive mixtures. This emphasises the need for components that retain or enhance the conductivity of the fuel cells at lower temperatures. The main challenge being faced today is the electrolytic component of the fuel only being able to operate at much higher temperatures. Not only does this pose a risk to the use of hydrogen as a fuel, but also introduces the need for a material that won't undergo significant thermal transformations. Therefore, optimising the electrolyte has been of great interest in energy research.

1.9 Components in Energy Devices

Energy devices are made up of three main components: two electrodes (cathode and anode), and the electrolyte. The energy is usually stored in the electrolyte and transfers charge to the anode, through which electrons travel to the load, back down the cathode and recycled back into the electrolyte (Figure 1.12).

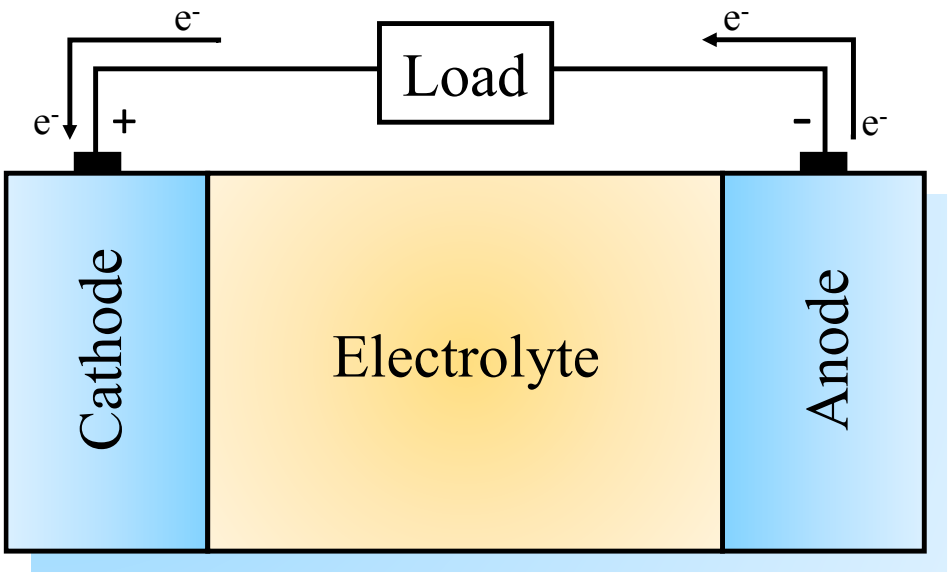

Figure 1.12: Diagram of a typical energy device illustrating the flow of electrons.

Cathodic Materials

In a battery, the cathode is the electrode where reduction occurs during the discharge cycle. As with all components in a cell, it must be chemically and structurally compatible with the electrolyte and anode materials to ensure long-term stability and efficiency. A few cathode materials include lithium cobalt oxide ($LiCoO_2$) [85], lithium iron phosphate ($LiFePO_4$) [86], and lithium manganese oxide ($LiMn_2O_4$) [87] in lithium-ion batteries, and lead (IV) oxide (PbO_2) in lead-acid batteries [88].

Anodic Materials

The anode is the electrode where oxidation occurs during the discharge process. The choice of the anode material affects the energy density (how much energy the device can store) and the power density (how quickly the device can deliver energy). Graphite is often used in lithium-ion batteries as it's favoured for its ability to intercalate lithium ions. Metallic lithium has the highest specific capacity, but they face challenges due to safety concerns and durability issues due to dendrite formation. Silicon-based anodes have a much higher capacity compared to graphite but suffers from substantial volume expansion while charging, which can lead to structural degradation [89].

Electrolytes

Electrolytes transfer charge in the form of ions between the anode and cathode of an energy storage or conversion device. This ionic conductivity is essential for the device's operation as it facilitates the storage of electrochemical energy and the circulation of charge in energy devices while preventing a short circuit. A good electrolyte should be chemically stable and inert towards other components of the cell at operating voltages and temperatures [90]. Electrolytes can take the form of a liquid, solid or polymeric state, all of which present with have benefits and drawbacks.

Liquid electrolytes are commonly found in lead-acid and lithium-ion batteries, and are typically solutions of salts, acids, or bases in organic solvents or water. They offer high ionic conductivity but often have issues with leakage and flammability [91].

Solid electrolytes are used in solid-state batteries and fuel cells; they include ceramics and glassy materials which can withstand high operating temperatures – a must in elevated temperature operated fuel cells [92]. While they offer improved safety and potentially higher energy densities, they face challenges with ionic conductivity and complexity in manufacturing.

Polymer electrolytes are found in gel and some lithium-ion batteries. Polymer electrolytes are safer than liquid ones and can be shaped into flexible films, but they usually have lower conductivity [93].

Solid electrolytes could potentially solve existing problems with liquid phase electrolytes that are currently being used in supercapacitors [94]. Several solid-state materials that can be used as solid-state electrolytes are already known and they include various metal oxides [95], borates [96], and sulphides [97]. However, these chemicals suffer from drawbacks such as, poor chemical stability [94], low ionic conductivity, and low specific capacitance [98]. To overcome these drawbacks, novel electrolytic materials must be developed that will reduce the

frequency of these drawbacks while simultaneously lowering manufacturing costs. Metal pyrophosphates have shown great potential due to their cost of synthesis, layered morphology reversibility, and high ionic conductivity which are desirable characteristics for energy devices [99].

This chapter has highlighted the importance of ceramics, particularly pyrophosphates, in energy storage and conversion devices. It has explored the properties and applications of metal pyrophosphates, emphasizing their role in different scientific and engineering fields. It also investigated how metal pyrophosphates are synthesised, characterised, and improved through doping for use in energy devices like supercapacitors and fuel cells. This sets the stage for further research aimed at using metal pyrophosphates to advance energy storage technologies and improve energy device efficiency.

1.10 Aims and Objectives

Based on the literature evidence presented here, there are numerous potential elemental combinations that produce doped metal pyrophosphates that are yet to be examined. Titanium pyrophosphate (TiP_2O_7), zirconium pyrophosphate (ZrP_2O_7), and hafnium pyrophosphate (HfP_2O_7) are all tetravalent metal pyrophosphates that crystallize in the cubic space group – $Pa\bar{3}$ [100]. Cubic-TiP_2O_7, -ZrP_2O_7 and -HfP_2O_7 are, therefore isostructural and possess similar chemical and physical properties.

While these three compounds display similar characteristics, we chose to focus our efforts on a study of the synthesis and characterization of a series of doped HfP_2O_7 compounds with the general formula $La_xHf_{1-x}P_2O_7$. This choice was based on the relatively unexplored nature of this compound presenting an opportunity to investigate its unique properties. Two sample sets (Group 1 and 2) of this material were synthesized via two variations of the sol-gel method with the intention of increasing the surface area of the resulting samples. While both sample sets were synthesized using the sol-gel method, the first sample set incorporated an additional filtering and drying step that preceded the final annealing step.

Therefore, we investigated the effect of doping HfP_2O_7 with La^{3+}, in the doping range of 1 – 5 wt%. This doping range was chosen to reduce the likelihood of a different phase or multiple phases arising. La^{3+} was chosen as it is found to the immediate left of Hf on the periodic table. Doping with an element of similar size has good potential for compatibility in the material without extensively modifying the parent crystal structure while still altering its physicochemical properties. Therefore, to study and test these hypotheses we set out to complete the following objectives:

1. The synthesis of phase pure and lanthanum-doped hafnium pyrophosphates ($La_xHf_{1-x}P_2O_7$) by two variations of the sol-gel method.

2. Following synthesis, the samples will be characterized in terms of their chemical, structural and electrochemical properties. The characterization methods used included powder x-ray diffraction (PXRD), ^{31}P magic angle spinning solid state nuclear magnetic resonance spectroscopy (^{31}P MAS ssNMR), pair distribution function (PDF), differential thermal analysis (DTA), thermal gravimetric analysis (TGA), Fourier transform infrared spectroscopy (FTIR), high-resolution transmission electron microscopy (HR-TEM), and potentiometric electrochemical impedance spectroscopy (PEIS).

3. The information obtained from the various characterization techniques were used to study and describe the dopant effect on the parent hafnium pyrophosphate material with regards to its structural, chemical, thermal, and electrochemical properties.

Chapter 2: Methodology

2.1 Synthesis

Part 1 – Group 1 and 2

The synthesis of phase pure and lanthanum-doped hafnium pyrophosphates was carried out using the sol-gel method. 30 mℓ of deionised water was added to 1.7945 g of hafnium (IV) chloride ($HfCl_4$) in a 100 mℓ beaker, followed by the addition of 10 mℓ of isopropanol to the $HfCl_4$ solution. Subsequently, the stoichiometric equivalent, 1.671 g of ammonium phosphate ($(NH_4)_3PO_4$) was dissolved in 30 mℓ deionised water in a separate beaker. Both reaction mixtures were then heated to 80 °C on a hot plate monitored by a thermometer. Following dissolution of both solutions, the $(NH_4)_3PO_4$ solution was then added slowly to the $HfCl_4$ solution with continuous stirring using a stirrer bar. For the samples doped with lanthanum (doping range of 1 – 5 %), stoichiometric amounts of lanthanum (III) nitrate hexahydrate ($La(NO_3)_3 \cdot 6H_2O$) were added to their respective $HfCl_4$ solutions before the addition of the $(NH_4)_3PO_4$ solution.

Part 2 – Group 1

Group 1's samples were then filtered to remove excess solvent. The samples were placed in a muffle furnace and heated at a rate of 10 °C/min and annealed at 900 °C for 1 hour.

Part 2 – Group 2

Group 2's samples were left to cool overnight, allowing excess solvent to evaporate. Once dried, the samples were placed in a muffle furnace and heated at a rate of 10 °C/min and annealed at 900 °C for 1 hour.

Doping quantities used in both Group 1 and 2's synthesis are listed in Table 2.1 on the following page.

Table 2.1: Mole and mass percentages of HfP_2O_7 and dopant starting materials.

Sample Number	**Sample Name**	**Doping (wt%)**	**$La(NO_3)_3 \cdot 6H_2O$ (g)**	**La added ($\times 10^{-4}$ mol)**
Phase Pure	HfP_2O_7	N/A	N/A	N/A
1	$La_{0.01}Hf_{0.99}P_2O_7$	1	0.03149	0.727
2	$La_{0.02}Hf_{0.98}P_2O_7$	2	0.06362	1.469
3	$La_{0.03}Hf_{0.97}P_2O_7$	3	0.09641	2.226
4	$La_{0.04}Hf_{0.96}P_2O_7$	4	0.1299	3.000
5	$La_{0.05}Hf_{0.95}P_2O_7$	5	0.1641	3.789

The synthesis of the $La_xHf_{1-x}P_2O_7$ series of compounds is summarized in the following reaction scheme:

$$HfCl_{4\,(s)} + C_3H_5OH_{\,(l)} + La(NO_3)_3 \cdot 6H_2O_{\,(s)} + (NH_4)_2HPO_{4\,(s)} + H_2O_{\,(l)}$$

(Hot plate at 80 °C)

↓

$La_xHf_{1-x}(PO)_{\,(aq)}$ (intermediate)

(Drying oven at 100 °C for 24 hours)

↓

$La_xHf_{1-x}(PO)$ (amorphous)

(Furnace at 900 °C for 1 hour)

↓

$La_xHf_{1-x}P_2O_{7\,(s)}$

A visual depiction of the synthetic procedure is illustrated in Figure 2.1 on the following page.

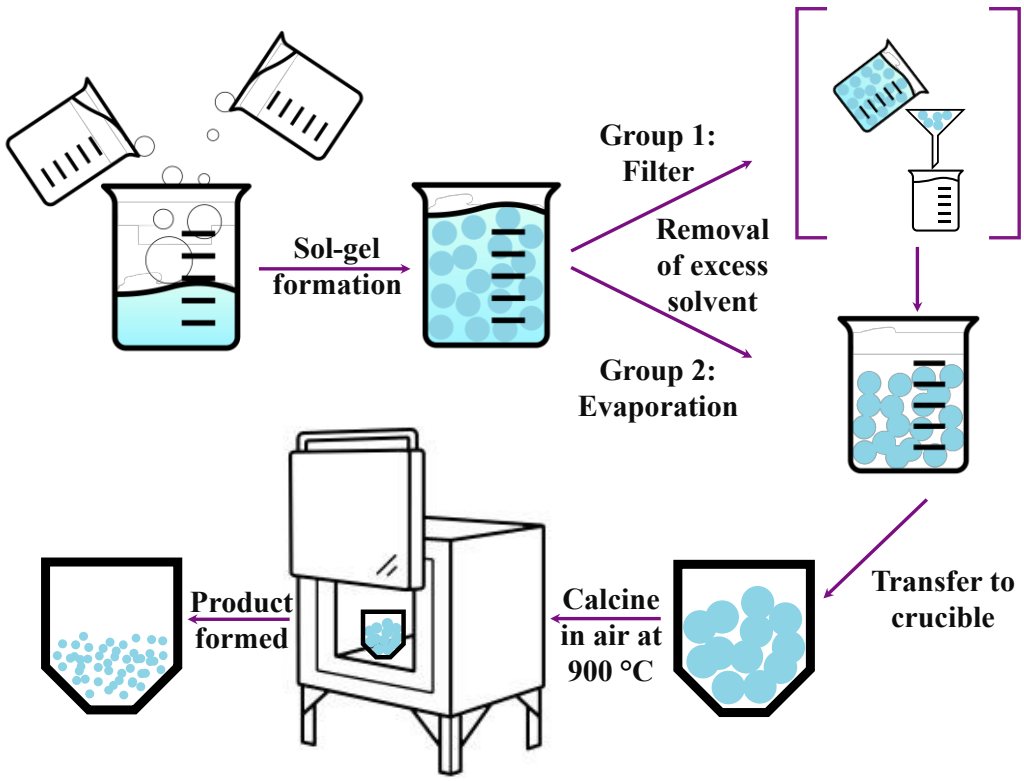

Figure 2.1: Diagram illustrating the method of synthesis of both groups of $La_xHf_{1-x}P_2O_7$.

2.2 Characterization

Following synthesis of the materials, PXRD, Pair Distribution Function (PDF), ^{31}P MAS ssNMR, and FT-IR data were collected. These characterization techniques provide insight into the chemical composition and crystal structure of the materials synthesized. Further characterization was then done using HR-TEM to provide further details on the crystallite size, grain boundaries, and chemical composition of the materials. Potentiometric electrochemical impedance spectroscopy (PEIS) was then performed on the materials to test their ionic conductivity. To examine the temperature stability of the materials, thermal gravimetric analysis (TGA) and differential thermal analysis (DTA) were measured on these materials.

Ex situ PXRD: Bruker D2

Ex-situ PXRD data were collected on a Bruker D2 diffractometer. The diffractometer was equipped with a monochromated Co-Kα radiation source (λ = 1.78897 Å). PXRD data was collected in the 2θ angular range from 5 – 60 °2θ, with a step size of 0.026 °2θ, scan time of 96 sec/step for a total acquisition time of 28 minutes per dataset. Samples were flat packed onto Si (111) zero x-ray background single crystal wafers and the surface of the sample smoothed using a smooth glass slide.

Magic Angle Spinning Solid-state Nuclear Magnetic Resonance (MAS ssNMR)

^{31}P MAS ssNMR spectra were obtained using a BRUKER AVANCE III spectrometer operating at 7 T and employing a double resonance MAS probe. Each sample was loaded into a H14355 VL 4/3 106 µℓ sample rotor. The spectrometer frequency was set at 5 and 10 kHz with a spectral resolution of ± 3 Hz.

Pair Distribution Function

PDF data was collected on the ID11 Beamline at the ESRF Synchrotron. Its energy range is 18.0 – 140.0 keV, and its minimum and maximum beam size is 0.2 × 0.07 µm^2 and 1200.0 × 1000 µm^2, respectively.

Fourier Transform Infrared Spectroscopy (FT-IR)

FTIR analyses were executed on a Bruker Tensor 27 FT-IR with a spectral range of 7500 - 370 cm^{-1} using a standard KBr beamsplitter. The instrument resolution was < 1 cm^{-1} with a wavenumber and photometric accuracy better than 0.01 cm^{-1} at 2000 cm^{-1} and 0.1 % T, respectively. The interferometer used was the RockSolid^{TM}. The instrument's scan speed lies between 2.3 and 20 kHz, and its detector was a DigiTect^{TM} detector system with high sensitivity. About 50 mg of each sample was analysed on the instrument without any prerequisite sample preparation.

Transmission Electron Microscopy (TEM)

TEM images were captured on an FEI Tecnai T12 TEM with an operating voltage range between 20 and 120 kV. Magnifications reach up to 700 000 times. The instrument uses a Gatan MSC794 CCD camera for imaging, and a video camera for video recording. It also has an energy dispersive X-ray spectroscopy (EDS) system.

Differential thermal analysis (DTA) and thermogravimetric analysis (TGA)

DTA and TGA data were measured concurrently using a Perkin Elmer Simultaneous Thermal Analyzer (STA) 6000. The instrument was calibrated using an indium reference standard. Data was collected for each sample from 30 ˚C to 900 ˚C and while cooling from 900 ˚C to 30 ˚C, at a rate of 10 ˚C.min^{-1} per minute in nitrogen. The baseline was determined by loading and collecting data on an empty ceramic crucible using an identical heating profile. The analysis was performed using between 12 mg and 20 mg of each sample.

Electrochemical Characterisation

Approximately 150 mg of each sample was prepared for potentiometric electrochemical impedance spectroscopy (PEIS) by pressing them into pellets using an 8 mm diameter stainless steel die. Each sample was pressed for 10 minutes at 1 tonne of pressure. The pellets were then sintered in air at 900 ˚C for 6 hours. Finally, the pellets were then coated on both faces with a layer of gold, 10 nm thick.

Ex-situ PEIS analyses were then performed on a BioLogic VMP-300 with an EIS board. A frequency range of 1 MHz to 1 kHz was used to collect the data on a logarithmic scale at open circuit potential (OCP). An amplitude of 20 mV was established for the signal to reduce noise.

2.3 Data Reduction and Interpretation

For all PXRD data presented, the crystalline phase identification was done using DIFFRAC.EVA (Version 4.2. Release 2016) using the crystallography open database (COD) (Release 2020). Phase analysis was done using the Rietveld method as implemented in Bruker AXS TOPAS software (Version 5, 2014). Phase analysis of PDF data was done on pdfGUI. NMR data processing was done using MestReNova Software (Version 14.3.0). FTIR spectra were processed and analysed using OPtics User Software (OPUS) (Version 6.5). TEM Images were analysed using ImageJ image processing software. STA measurements were collected on Pyris. PEIS spectra were plotted and analysed using EC Lab (Version 11.3, 2018), and all data were plotted in Python using the matplotlib and numpy libraries.

Chapter 3: Structural Analysis

3.1 Powder X-Ray Diffraction

PXRD data collected on all 12 samples of $La_xHf_{1-x}P_2O_7$, showed a distinct difference between the samples of Groups 1 and 2 – this difference being the degree of crystallinity of the materials.

$La_xHf_{1-x}P_2O_7$ materials obtained from group 1 all showed an increased affinity towards an amorphous nature, with distinguishable peaks only present in the HfP_2O_7 and $La_{0.01}Hf_{0.99}P_2O_7$ samples, with no crystallinity observed in the 2-5% doped samples (Figure 3.1). This would suggest that the 2% doping concentration of La^{3+} is the threshold before short-range order is highly prevalent in the materials. While a Rietveld analysis could be performed on the materials, their lack of crystallinity would prove useless as there are no Bragg peaks to match to a structure model. Therefore, since these samples lack crystallinity and therefore lack long range order, we will instead examine the local order of the materials using a pair distribution function analysis.

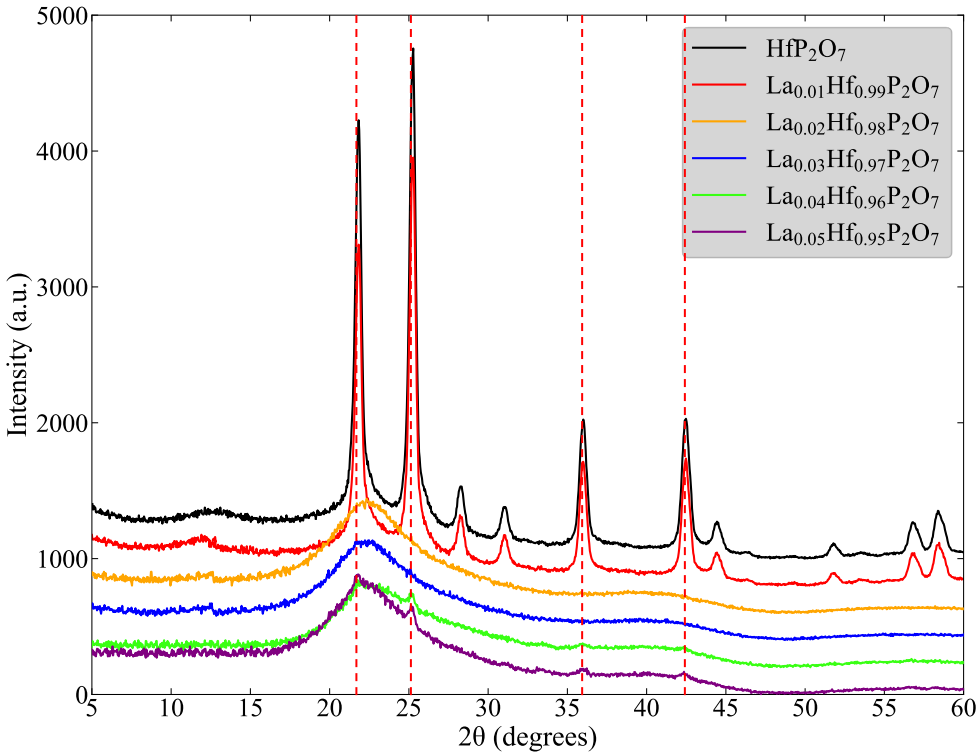

Figure 3.1: PXRD patterns of $La_xHf_{1-x}P_2O_7$ stacked for a comparative view of Group 1's materials – crystalline peaks in amorphous phases = ----.

Unlike group 1's PXRD data, group 2 showed a high degree of crystallinity in all samples in the series (Figure 3.2). The PXRD data collected on all samples up to and including the $La_{0.04}Hf_{0.96}P_2O_7$ showed that there were no apparent changes in the phase of the materials through to $La_{0.04}Hf_{0.96}P_2O_7$. There are slight intensity differences, which was examined in the Rietveld Refinements (Figure 3.3). The PXRD data collected on sample $La_{0.05}Hf_{0.95}P_2O_7$, however, showed evidence of new features arising as small, broad "peaks". These results that implied a crystalline nature in Group 2's materials suggested that the additional filtering and drying step used for the synthesis of the samples in Group 1, may inhibit the process of crystallization.

The data suggested that while filtering the gel removed the solvent, it may have disturbed the colloidal network formed in the sol-gel process, thus giving rise to less homogeneity in the remaining gel, especially with the addition of the dopant – as evident in Group 1's PXRD patterns (Figure 3.1).

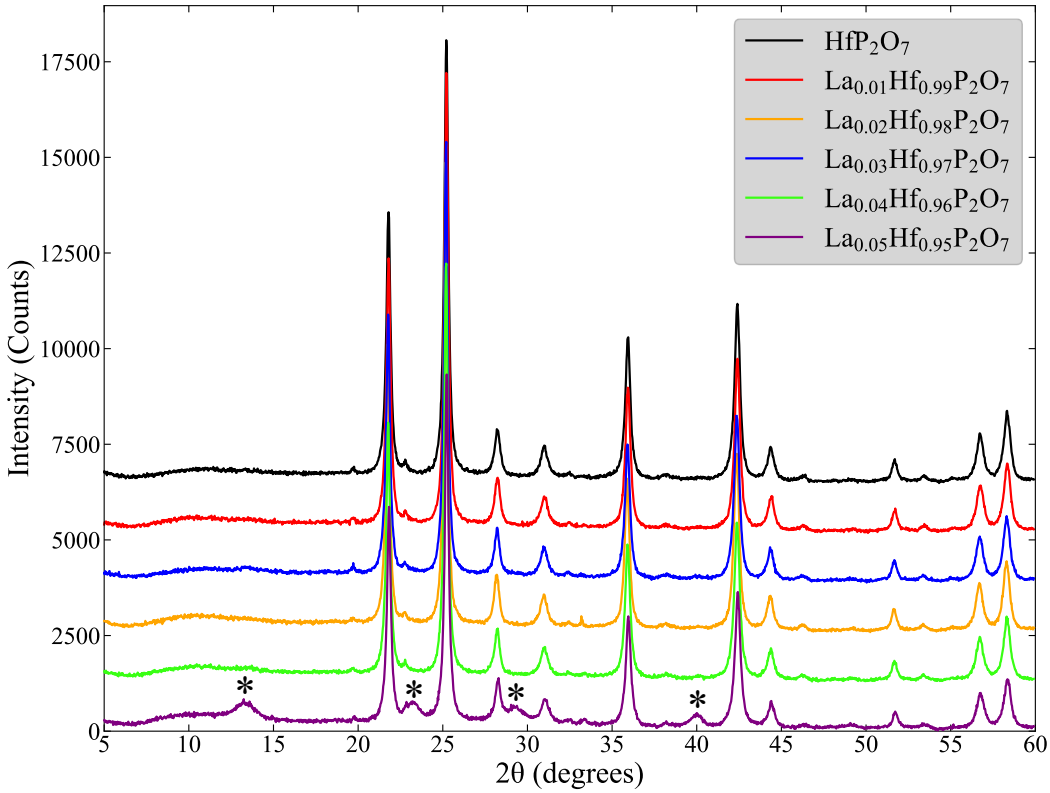

Figure 3.2: PXRD patterns of $La_xHf_{1-x}P_2O_7$ stacked for a comparative view of Group 2's materials – unidentified phase = *.

To examine the crystallinity and structural parameters of the materials, Group 2's samples were analysed via Rietveld refinement (Figure 3.3). The refinements showed a good fit of the structure model (Figure 3.4 – ICSD code 172201) to the experimental data, with an average goodness of fit (GoF) of 1.93 and an average weighted Residual profile factor (R_{wp}) of 6.645.

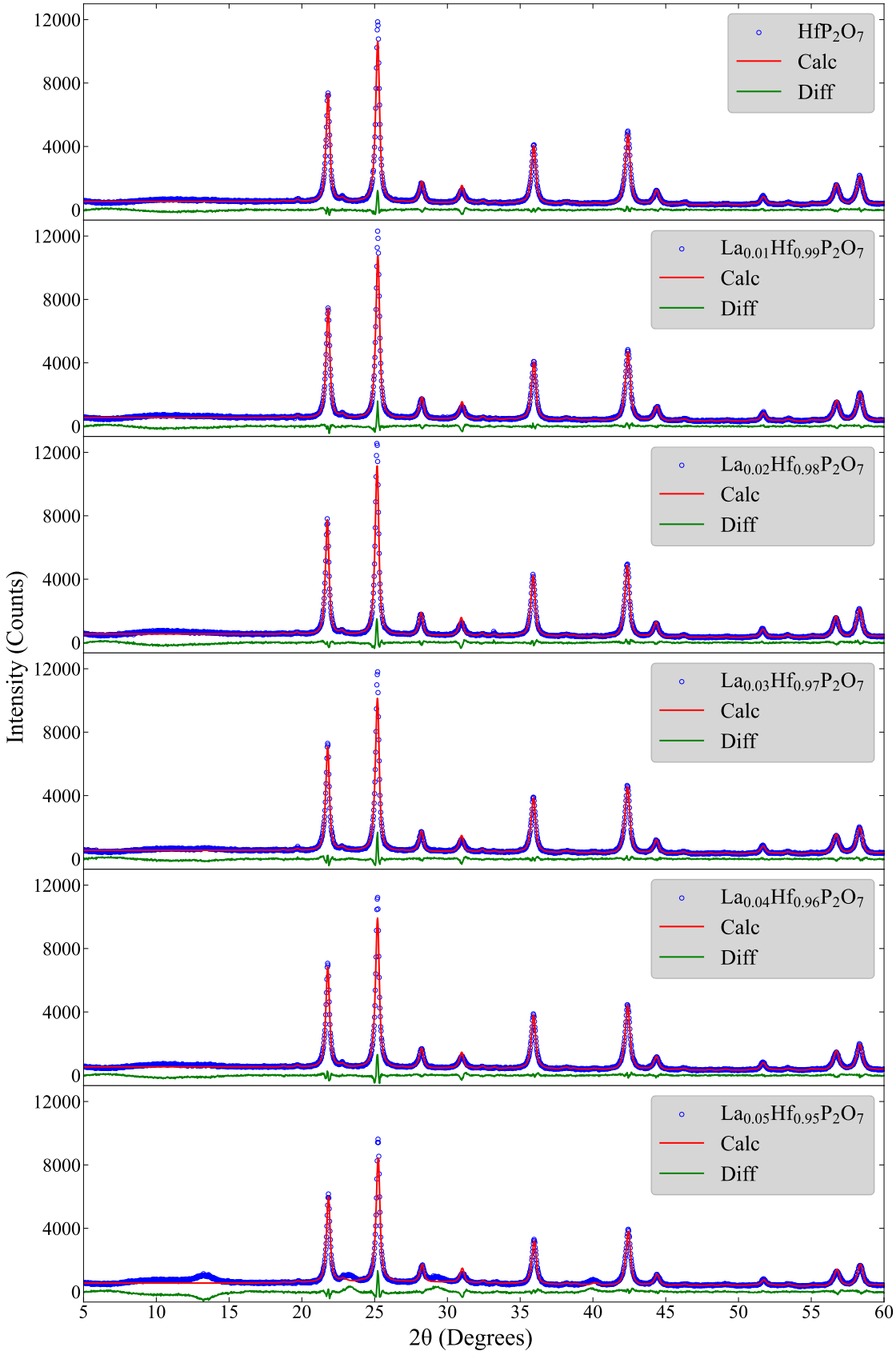

Figure 3.3: Stacked PXRD Rietveld refinements of $La_xHf_{1-x}P_2O_7$ from Group 2, blue = obs, red = calc, green = diff.

From these refinements, the lattice parameters were determined (Table 3.1). When compared to that of the original structure model (Figure 3.4), a good correlation of values was observed as seen by the model's lattice parameters.

Table 3.1: PXRD Refinement results of Group 2's samples and the orthorhombic structure model's arrangement it adopts, comparing lattice parameters, GoF, and R_{wp} values.

Sample	**Lattice Parameters (Å)**		
	a	**b**	**c**
HfP_2O_7	24.6210096	24.6192516	24.6209046
$La_{0.01}Hf_{0.99}P_2O_7$	24.6171811	24.6201910	24.6170262
$La_{0.02}Hf_{0.98}P_2O_7$	24.6163842	24.6179673	24.6181731
$La_{0.03}Hf_{0.97}P_2O_7$	24.6206313	24.6188393	24.6183744
$La_{0.04}Hf_{0.96}P_2O_7$	24.6187484	24.6231652	24.6180233
$La_{0.05}Hf_{0.95}P_2O_7$	24.6222188	24.6186920	24.6186384
***Pbca* model**	24.6520000	24.6296000	24.6510000

	Average crystallite size (nm)	**GoF**	**R_{wp}**
HfP_2O_7	47.2	1.66	5.69
$La_{0.01}Hf_{0.99}P_2O_7$	47.8	1.71	5.83
$La_{0.02}Hf_{0.98}P_2O_7$	52.4	1.78	6.08
$La_{0.03}Hf_{0.97}P_2O_7$	50.9	1.77	6.13
$La_{0.04}Hf_{0.96}P_2O_7$	45.9	1.78	6.19
$La_{0.05}Hf_{0.95}P_2O_7$	50.2	2.90	9.95

While the PXRD data does appear similar for each sample in Group 2, the 5% doped sample appears to give rise to an additional, unidentified phase, hence its bad GoF value. This implies that the dopant is present in the parent HfP_2O_7 crystal, however, from the 5% doped sample, either substitution had reached its threshold, or a new phase of $La_xHf_{1-x}P_2O_7$ arose. The possibility of an existing phase like lanthanum or hafnium oxide, or lanthanum or hafnium phosphate were examined

by a Rietveld analysis, but no match was found. However, given the lack of detail in the PXRD data we need to study local order differences to determine the effects of substitution while also itself providing further evidence of proof of lattice substitution by La^{3+}. Therefore, ^{31}P MAS ssNMR data was collected on all samples to investigate the changes to the phosphate tetrahedral structure within these materials.

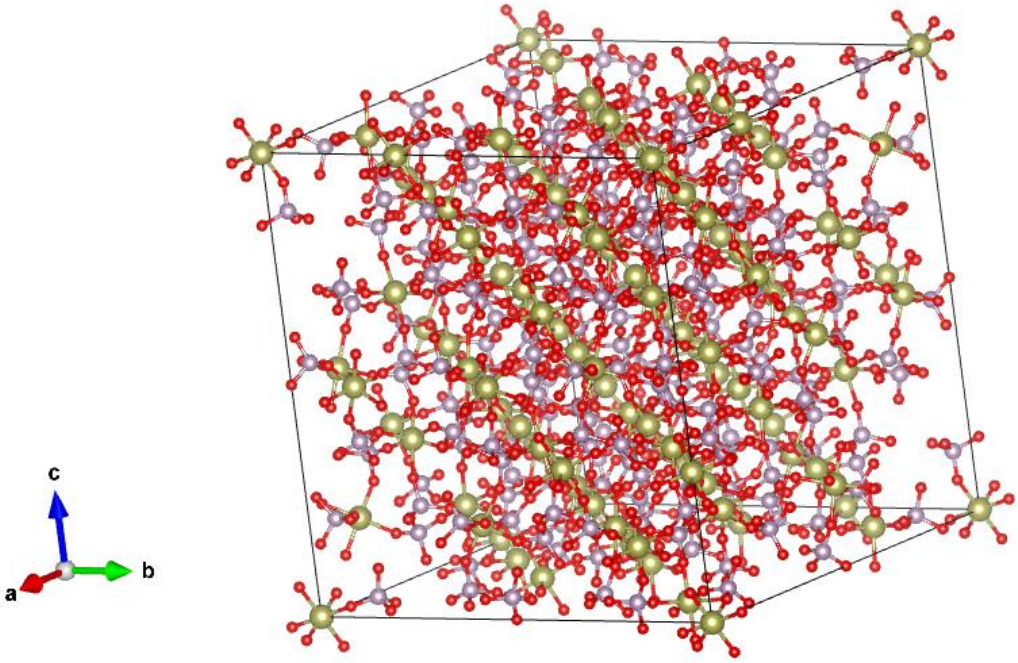

Figure 3.4: Orthorhombic structure model of HfP_2O_7; space group = *Pbca*; model is an expansion of the cubic structure ($Pa\bar{3}$) but a ≠ b ≠ c – ICSD code 172201.

3.2 ^{31}P MAS ssNMR analysis

^{31}P MAS ssNMR was used to investigate/look for any changes in the spectra that were associated with a change in the P atom environment corresponding to an increase in La^{3+} dopant concentration. Data was collected on both samples sets. In both groups, peaks at -5 ppm (PO_4^- moiety [101]), -23 ppm (P-O-P moiety [102]), and -35 ppm (P-O-P moiety [102]) were demarcated by ✦, ✦, ✦, respectively.

Signals were observed between 67.102 and –111.91 ppm in the ^{31}P MAS ssNMR (Figure 3.5) in Group 1's sample. Considering the addition of La^{3+} in the samples, as the concentration of the lanthanum increases, the peaks shift downfield from the 2% doped sample onwards. This shift may be a result of the incorporation of the La^{3+} ions inducing a chemical shift perturbation [103] by disrupting the local electronic environment around the phosphorus atoms. This perturbation can lead to reduced shielding and, therefore, a downfield shift in the ^{31}P MAS ssNMR peaks [104], which, although subtle, is observed in Figure 3.5.

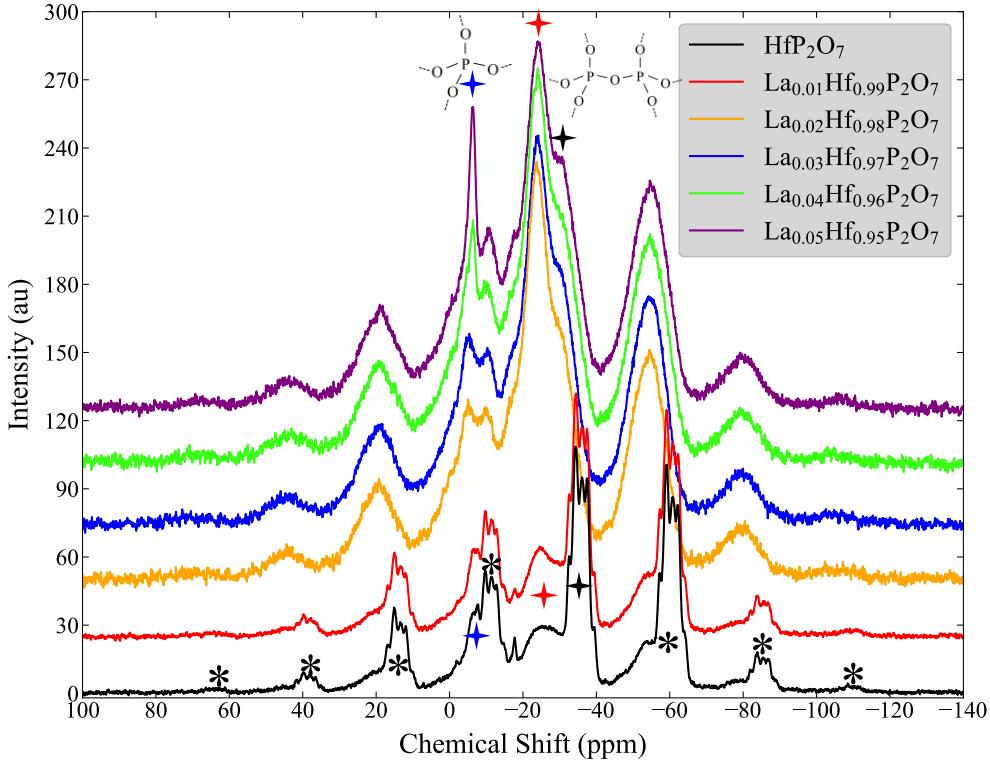

Figure 3.5: ^{31}P MAS ssNMR plots of Group 1 superimposed over one another – spin rate of 5 kHz; main signals = ✦, ✦, ✦; respective spinning side bands = *, *, *.

In addition to the shifting of peaks, the common broadening of peaks in MAS ssNMR due to anisotropic effects [105] are seen in all spectra. While broadening of peaks is expected, the excessive broadening can be attributed to certain properties of the samples, including inhomogeneities introduced by the increasing concentration of dopant [106], and, more so the amorphism (established in the PXRD patterns and PDF analysis). This amorphism is potentially a result of the filtering step disrupting the colloidal network formed in the gel [107], thereby reducing the long-range order in the final product, therefore supplementing to the inhomogeneity in the materials.

In addition to the broadening, the spinning sidebands presented with a "roofing" effect which is a result of the overlapping of neighbouring signals. It is important to note that from the 2% doped sample onwards, there is a significant change in the spectra, showing broader and less resolved signals, resulting in merging of signals, and a downfield shift in the signals originally observed at ~35 ppm by approximately 10ppm. This signified that the addition of La^{3+} may be causing these noticeable changes by changing the local electronic environment around the P atoms [108], either by a direct electron withdrawing effect, or by indirectly making the O atoms more electron withdrawing, de-shielding the P atoms in this environment.

Like Group 1's NMR data, signals between 66.537 and –132.060 ppm were also observed in Group 2's ^{31}P MAS ssNMR data (Figure 3.6). A noticeable difference in the data collected for each sample set was observed; however, this is mainly due to the difference in spinning speed giving rise to fewer spinning sidebands in Group 2's spectra. We also observed that there were no peak shifts in these spectra set which may be have been due to a higher degree in crystallinity [109] (established in the PXRD patterns in Figure 3.2), therefore lowering the probability of chemical shift perturbations from occurring due to its long-range order giving rise to fewer distinct local environments [103].

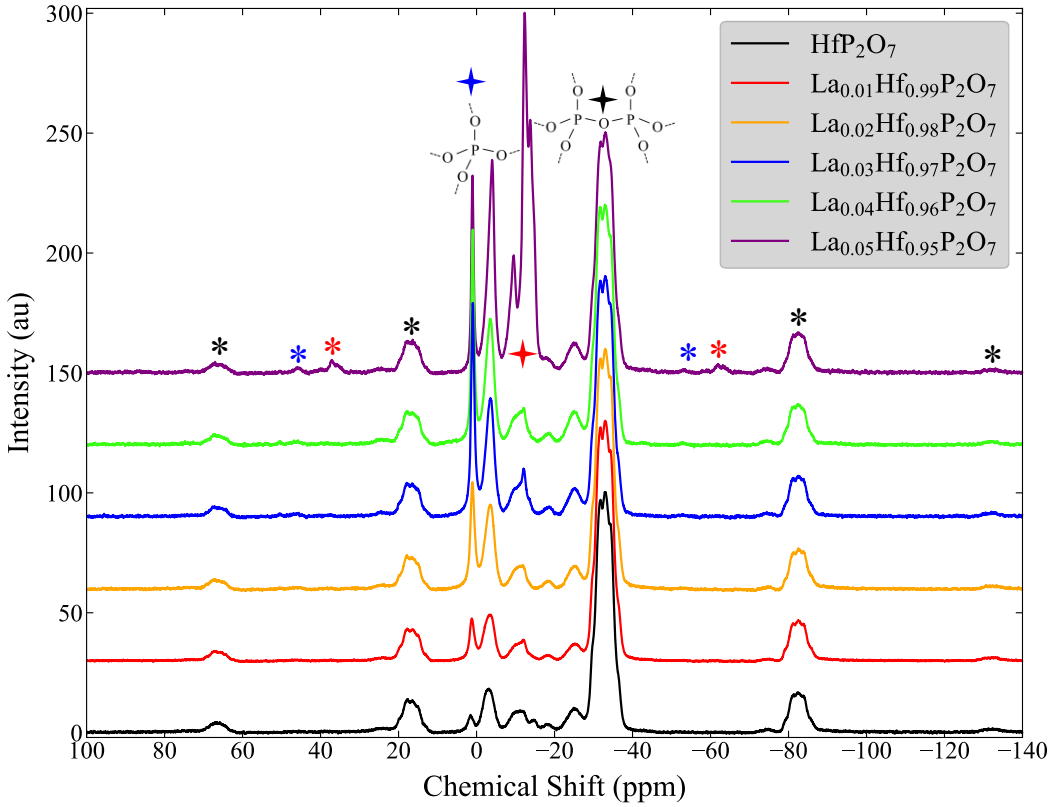

Figure 3.6: ^{31}P MAS ssNMR plots of Group 2 stacked – spin rate of 10 kHz; main signals = ✦, ✦, ✦; respective spinning side bands = *, *, *.

As mentioned previously, a very important aspect of MAS ssNMR is the common broadening of peaks resulting from anisotropic effects [105] arising from the varying atomic orientations expected in the solid-state. This was noticeable in Group 1's spectra (Figure 3.5), however this was far less pronounced in Group 2's spectra (Figure 3.6) – possibly due to its long-range order (fewer orientations, fewer distinct environments), however more so because of the difference in spinning speed which gave rise to fewer spinning sidebands, and therefore, less peak overlap. Different spinning speeds were used due to a miscommunication and with limited access to the solid-state NMR spectrometer, correction of this could not be completed in the restricted timeframe with the solid-state probe only being in use twice a year, one month at a time. Rectification of these results can be part of future studies.

Unlike in Group 1, further broadening with increasing dopant concentration was not observed in Group 2's spectra, supporting the presence of fewer distinct P

environments in the materials with a higher degree of crystallinity (less inhomogeneity [106]).

Apart from the discussed line broadening, the presence of spinning sidebands also complicates the spectra, as previously mentioned. They are not a result of coupling, but rather due to the samples being spun at a rate less than that of the anisotropic interactions [110], which is evident when comparing the amorphous samples' spectra to those of the crystalline samples (see Figure 3.5 and Figure 3.6) whose spinning rates were 5 kHz and 10 kHz, respectively – faster spin rate, fewer spinning side bands. In fact, the distance between the spinning sidebands in Figure 3.5 was approximately half that of the spinning sidebands of the data presented in Figure 3.6, which was to be expected. Spinning sidebands can also be a result of sample tubing not having perfect symmetry, generally giving rise to a higher relative intensity of spinning sidebands [111] observed in Group 1's NMR spectra (Figure 3.5). While these spinning sidebands did give rise to interpretation difficulties, they helped identify corresponding signals between Group 1 and 2's spectra.

Overall, ^{31}P MAS ssNMR provided some insight into the local chemical environments relating to the various orientations of the P atoms in $La_xHf_{1-x}P_2O_7$, however, to get a better understanding of the local structure of the materials, more so for Group 1's materials, pair distribution function data was collected.

3.3 Pair Distribution Function (PDF)

Results from the PDF data provide insights into the structural characteristics of Group 1, characterized by a presumed amorphous nature. The obtained data (Figure 3.7) revealed a lack of discernible long-range order from its short atomic range observed, therefore reinforcing the presumed amorphous nature of the materials in Group 1 [112].

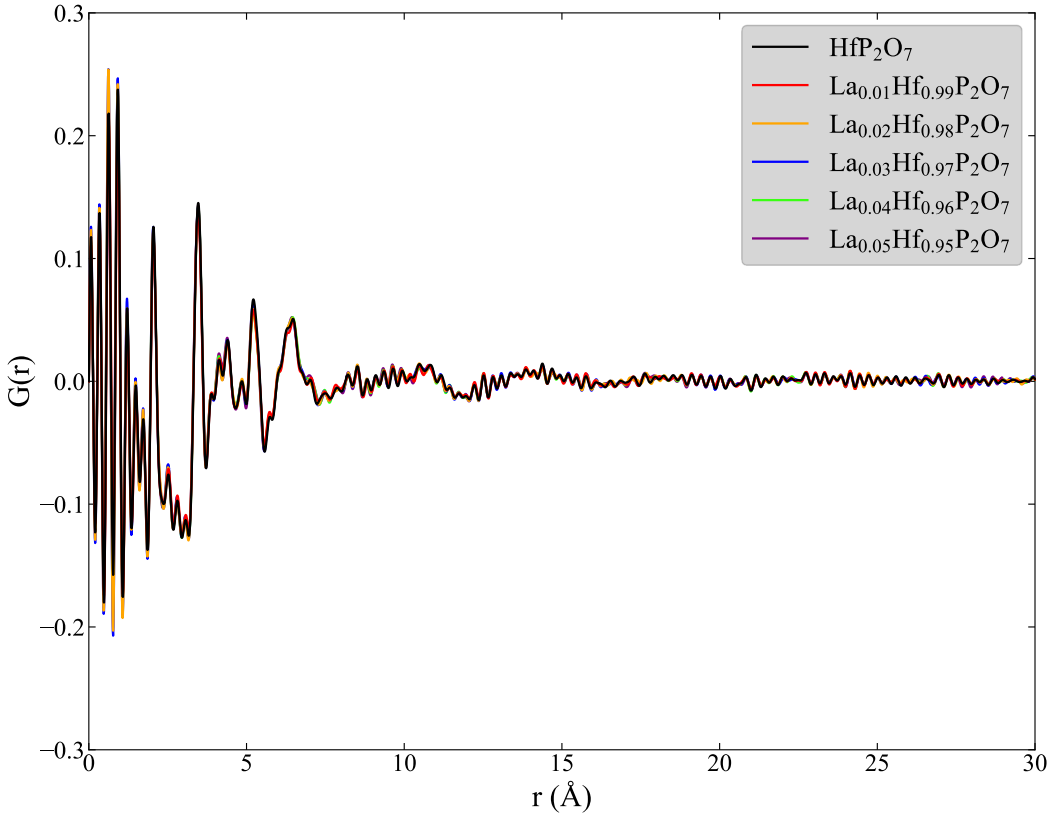

Figure 3.7: Layered plot of Group 1's PDF data, G(r) vs r, showing the radial distribution of atoms within Group 1's materials.

The PDF patterns compared very well with each other suggesting that the atomic distribution in the materials is analogous regardless of dopant concentration; this suggested they share local structural similarities. While the patterns are almost identical, there are slight discrepancies in the intensities of the signals. These are likely due to the samples being packed in a capillary with milligrams of sample and, therefore there is no way of ensuring the sample bed of all samples were consistent; this is an experimental limitation of using a capillary sample holder, which can subtly impact the intensities of the data.

Despite rigorous attempts, no structure model could fit Group 1's PDF data, as the models were inadequate for the short-range order evident in Group 1's materials. The short atomic range observed in the PDF therefore reinforces the presumed amorphous nature of the materials in Group 1 [112]. Since no structure model could be fit to Group 1's data, a direct, qualitative interpretation of the data was done. But, before this was done, Group 2's PDF data was interpreted first.

In contrast to Group 1, the PDF analysis of Group 2 (Figure 3.8) presents a different scenario. The data for this sample set exhibits a significantly higher degree of crystallinity compared to Group 1, as established by the PXRD data (Figure 3.3). The atomic pairs in Group 2 extend to a range of approximately 30 Å, in stark contrast to the limited range of around 6 Å observed in Group 1. This substantial difference in the PDF patterns is indicative of a more ordered atomic arrangement in Group 2, suggesting the presence of well-defined crystallographic structures within the materials.

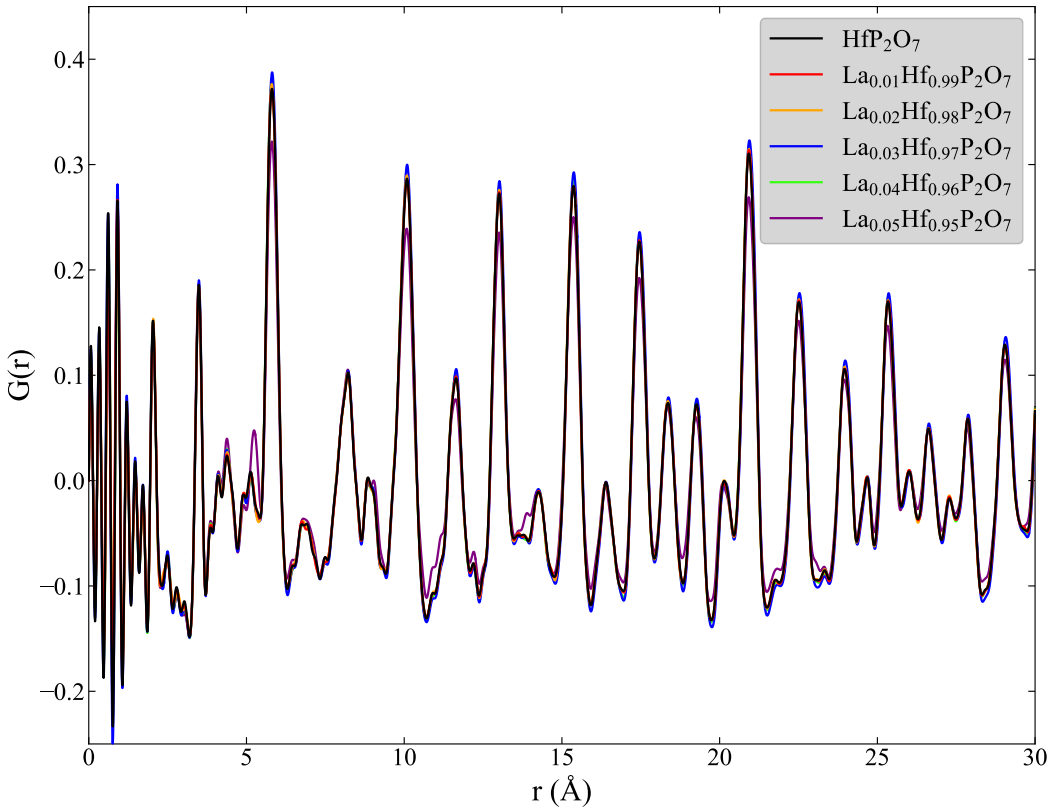

Figure 3.8: Superimposed plot of Group 2's PDF data, G(r) vs r in the range of 0 – 30 Å.

To further elucidate the crystalline nature of the materials in Group 2, a structure model was fitted and refined to the PDF data (Figure 3.9). This modelling process confirmed the existence of a crystal structure within the materials of Group 2. The refinement of the structure model not only supports the conclusion that Group 2 exhibits a longer range of order compared to Group 1, where little order was apparent, but also confirmed the structure refinement performed on the laboratory PXRD data (Figure 3.3). From these structure refinements, it can be concluded that the materials in Group 2 does not correspond to space group *Pbca*, but rather $Pa\bar{3}$, with lattice parameters a = b = c = ~8.22 Å (see Table 3.2 for precise values). While cubic and orthorhombic structures can be very different, this case seems to prove that the orthorhombic structure characterised by the PXRD data is just an expansion of the cubic structure due to the difference in the P–O–P angle. These findings emphasize the significance of PDF function analysis in characterizing the structure of a material, particularly in elucidating local structural order.

Table 3.2: pdfGUI refinement results obtained for Group 2 (Figure 3.9).

Compound	Space Group	Refined Unit Cell Parameters (Å) a = b = c	R_w of Fit
HfP_2O_7	$Pa\bar{3}$	8.221154	0.132978
$La_{0.01}Hf_{0.99}P_2O_7$		8.221915	0.132966
$La_{0.02}Hf_{0.98}P_2O_7$		8.220660	0.132483
$La_{0.03}Hf_{0.97}P_2O_7$		8.226482	0.133722
$La_{0.04}Hf_{0.96}P_2O_7$		8.221308	0.135010
$La_{0.05}Hf_{0.95}P_2O_7$		8.219627	0.159436
		Average	
		8,221858	0,137766
Trial Structure Model of HfP_2O_7	$Pa\bar{3}$	8.18	N/A

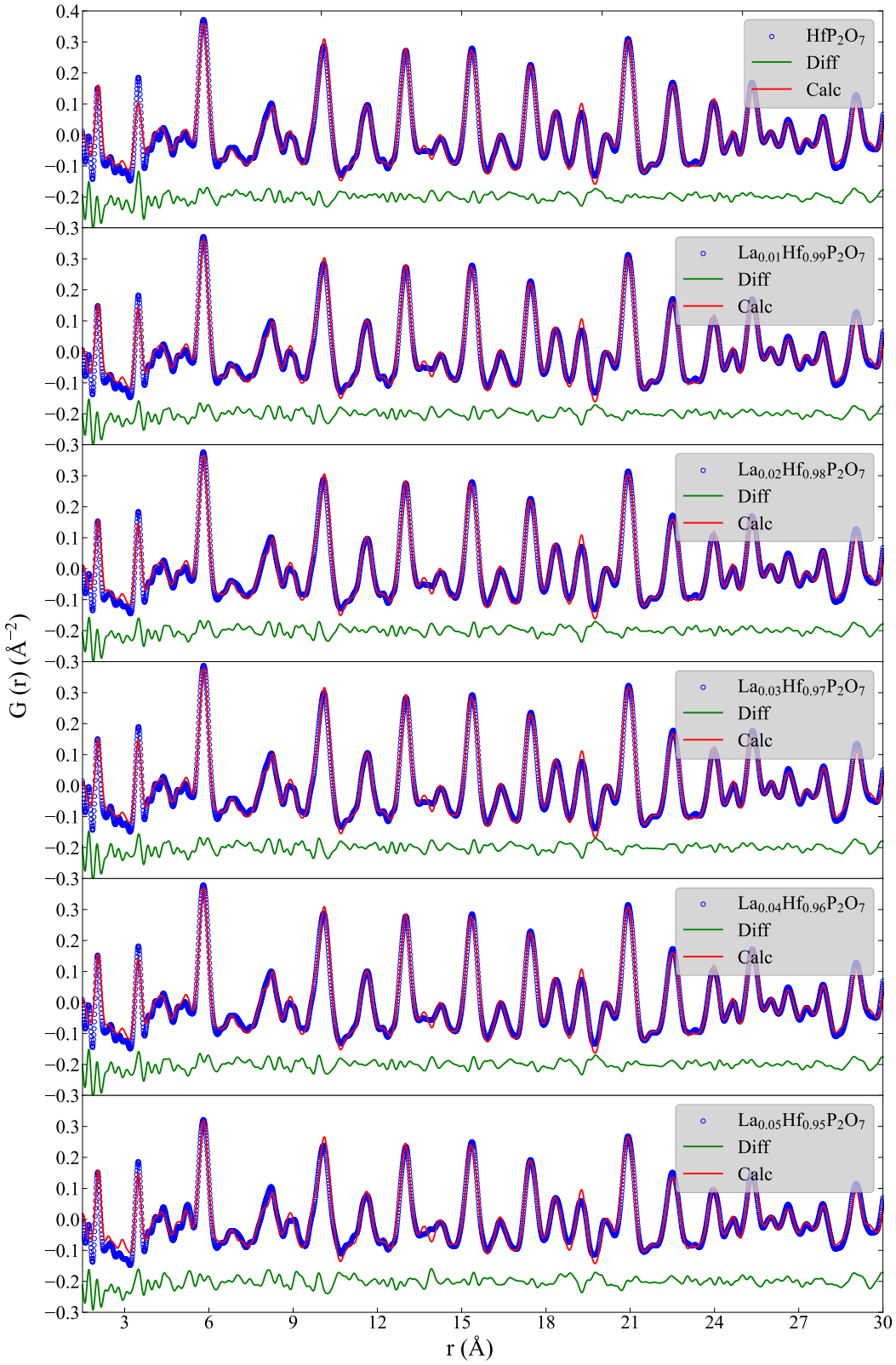

Figure 3.9: Stacked pdfGUI refinements of Group 2's PDF Data – blue = obs, red = calc (structure model), green = diff.

The atomic pairs were identified (Figure 3.9) and coupled to their corresponding PDF signals by determining their atomic distances using the structure model (COD ID – 5910283) and associating them with their PDF signals in Table 3.3.

Table 3.3: Identification of atomic pairs from the PDF Signals in Figure 3.9.

Atomic Pairs	r (Å)		Relative Error %
	Model	Experimental	
Hf – Hf	5.78413(0)	5.80343	0,33
Hf – O	2.01241(0)	2.03709	1,23
Hf – P	3.43463(0)	3.48881	1,35
P – O	1.53589(0)	1.47004	4,29

From Table 3.3, the atomic distance, r, for each atomic pair correlates very well to the original structure model, showing very small relative errors (< 5%) between the atomic pairs compared to the structure model, suggesting a good structural match. We also know from the R_w values (Table 3.2) that the difference between the experimental data and the structure model is very small, at an average of 13.8%, which, although higher than 10%, is good for a complex structure such as $La_xHf_{1-x}P_2O_7$. It can also be noted that as the dopant concentration increases, there is a slight increase in the R_w value, with the most significant increase (~2.4%) from the 4% to 5% doped sample. This agrees with the Rietveld refinements performed on the samples, where the 5% doped sample shows the most significant change in its R_w value. This may be indicative of the threshold between what's considered doping and substituting in HfP_2O_7, or even the threshold between a crystalline and an amorphous state – encouraged by the filtering step. However, PDF data does not provide enough information on this topic. ^{31}P MAS ssNMR data was then collected to gain more insight into the material that PDF and PXRD could not provide.

Then, as previously mentioned, Group 1's PDF data was qualitatively analysed by comparing it to Group 2's PDF data. This was done by comparing Group 1's PDF data to Group 2's PDF data in the region of 1 – 5.5 Å – the maximum comparable range of Group 1 and 2's data (Figure 3.10). Any peaks below 1 Å are considered

noise added after the Fourier transform of the data from reciprocal to real space. This is because most distances between atoms are not below 1 Å in length, and none of the atomic distances in $La_xHf_{1-x}P_2O_7$ are below 1 Å.

While few atomic pairs were observed in Group 1's PDF data (Figure 3.7), those which were observed were identified and tabulated in Table 3.4.

Table 3.4: Identification of atomic pairs from the PDF Signals in Figure *3.7*.

Atomic Pairs	r (Å)		Relative Error %
	Model	Experimental	
Hf – Hf	5.78413(0)	5.80345	0.33
Hf – O	2.01241(0)	2.03716	1.21
Hf – P	3.43463(0)	3.48872	1.55
P – O	1.53589(0)	1.51004	1.71

As observed in Figure 3.10, Group 1 and 2's materials' local structures match one another in the range of 1 – 5.5 Å, signified by the corresponding signals. This illustrates that both Group 1 and 2 are made up of samples of the same composition but different overall structure.

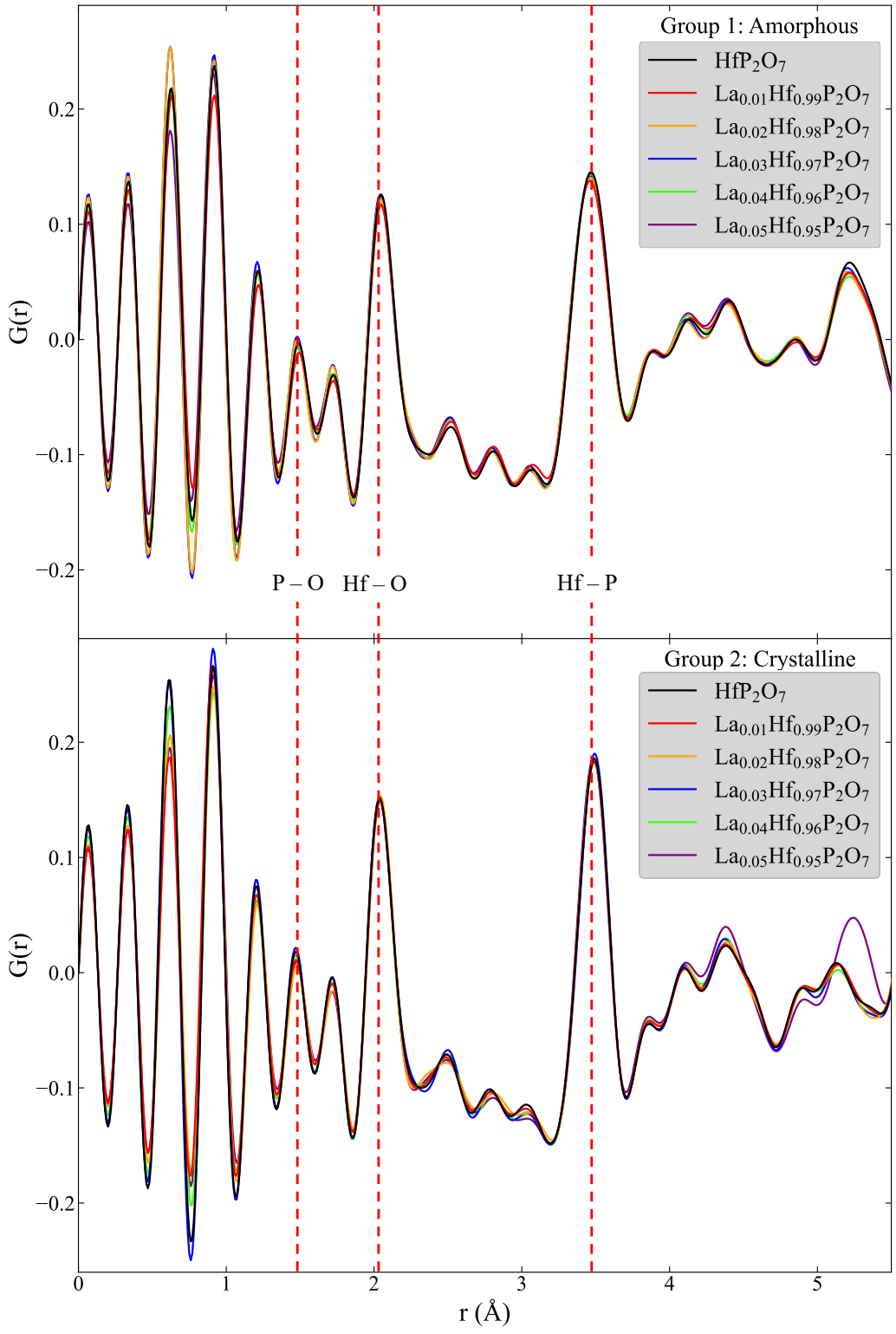

Figure 3.10: PDF data comparison of Group 1 and Group 2 - atomic pair correlations = - - -, P – O = distance between P and O atoms, Hf – O = distance between Hf and O atoms, Hf – P = distance between Hf and P atoms.

3.4 Fourier transform infrared spectroscopy (FTIR)

FTIR data was collected to identify the functional groups present in the materials. The FTIR spectra retrieved for both sample sets are not identical (Figure 3.11 and Figure 3.12), however, they both exhibit the characteristic peaks for the pyrophosphate functional group.

Group 1's FTIR exhibited a strong signal representing the asymmetric P – O stretches in the P–O–P moiety found in the pyrophosphate group, is observed in all the spectra at ~ 1000 cm^{-1} [113] (Figure 3.11). This is an out of phase stretch [113] – the P atoms bounce towards and away from the O atom interchangeably. Although there is no P=O in the lattice seen in the structure model (Figure 3.4), it can be expected in a pyrophosphate functional group [114] and is in fact seen in the spectra at ~1430 cm^{-1}. This weak signal at ~1430 cm^{-1} is representative of this P=O stretch [113] – usually this signal is much stronger, however, the strength, or lack thereof, of the signal may be attributed to the low concentration of this moiety in the material. Compared to the spectra of the doped samples, there is no significant shift in the signals, however there is a noticeable change in intensity. This change in intensity signifies variation in the concentration of the P–O–P functional group. Since this variation is minimal, it can be concluded that there is no major change in the functionalisation of the material when doped with lanthanum (III).

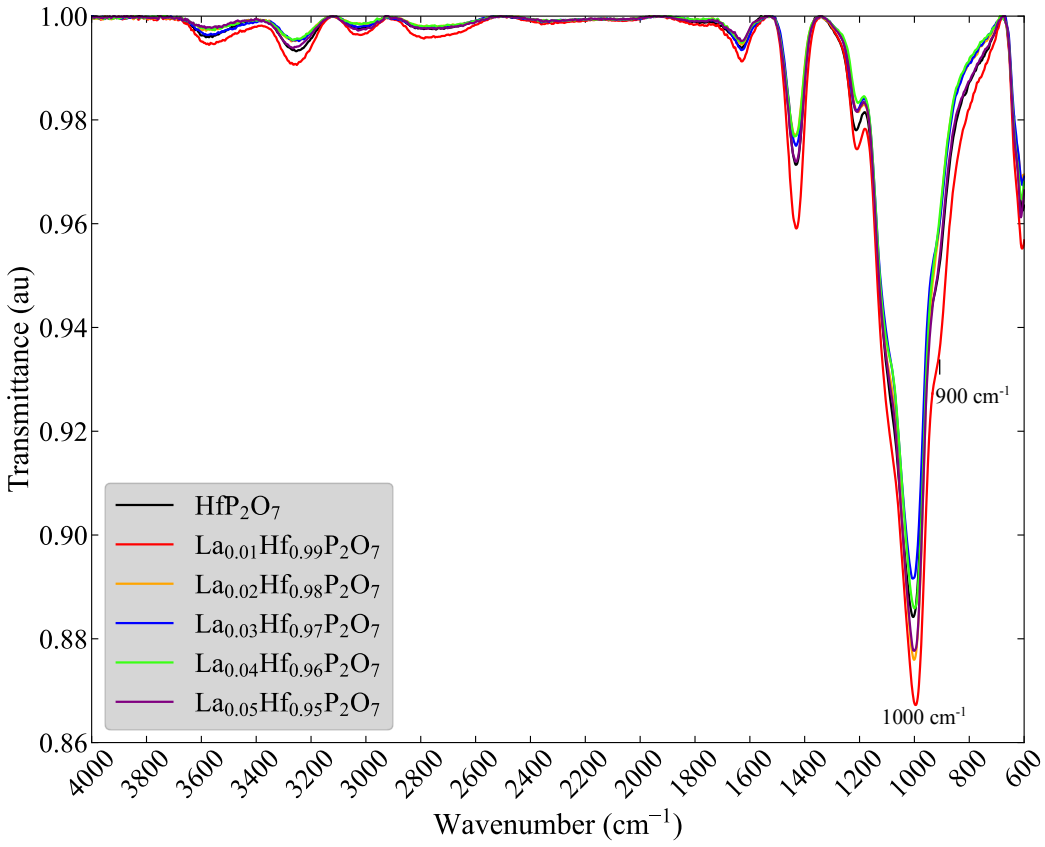

Figure 3.11: Superimposed spectra of Group 1's FTIR data – P-O-P asymmetric stretch at 1000 cm^{-1}; P-O symmetric stretch at 900 cm^{-1}.

While two distinct signals are usually expected in this region, it should be noted that the signal has shoulders from overlapping signals. The broadening of signals alludes, once again, to an amorphous nature exhibited by the samples in Group 1.

The right shoulder at ~900 cm^{-1} of the intense broad signal, suggested the overlapping of the expected band associated with the symmetric stretch from the P–O–P bridge [115]. The left shoulder of this band should correspond to the asymmetric stretching of the P–O bonds within the PO_3 moiety while the centre signal corresponded to their symmetric stretches [116]. The asymmetric stretch is observed at a higher wavenumber than the symmetric stretch as the energy required to shift the dipole moment during an asymmetric stretch is higher than what's required for the symmetric stretch [113] of the P–O bonds. The muted bands in the 3800 – 2800 cm^{-1} region, while not present in the compound, suggests the presence of hydroxyl groups. This suggests that water may adhere to the HfP_2O_7 particles.

Group 1's spectra characteristic signals observed in Figure 3.11 are tabulated in Table 3.5.

Table 3.5: Group 1's FTIR characteristic signals and their corresponding functional group vibrations

Sample	Wavenumber (cm^{-1})		
	P = O	P – O (– P) (asymmetric)	P – O (– P) (symmetric)
HfP_2O_7	1431,5	1005,2	605,65
$La_{0.01}Hf_{0.99}P_2O_7$	1430,2	996,76	607,7
$La_{0.02}Hf_{0.98}P_2O_7$	1433,8	1003,7	611,06
$La_{0.03}Hf_{0.97}P_2O_7$	1431,5	1007,1	606,6
$La_{0.04}Hf_{0.96}P_2O_7$	1436,4	1003,1	609,23
$La_{0.05}Hf_{0.95}P_2O_7$	1431,8	1003,3	611,62

The FTIR spectrum corresponding to Group 2 is shown in Figure 3.12. The symmetric and out-of-phase stretching frequencies of the PO_3 moiety in $P_2O_7^{4-}$ are observed as two intense signals at 1094,1 and 981,18cm^{-1} [116], respectively. A signal is observed at 746 cm-1, correlating to the symmetric stretching, experienced by the P–O–P bridge [115]. The frequency of the P–O–P bridge stretch is anticipated to be lower than that of the P–O stretch in the PO_3 as the P–O bond in the P–O–P bridge is weaker than that of the PO_3 group [115]. This can be supported by the fitted PDF data (Figure 3.9) which reveals shorter bond distances between the PO_3 P–O bonds compared to those within the P–O–P bridge. Noticeably, the bands found in the 3800 – 2600 cm^{-1} range in Group 1's FTIR spectra are absent in Group 2's FTIR spectra. This may suggest that Group 1's materials are hygroscopic, and Group 2's are not.

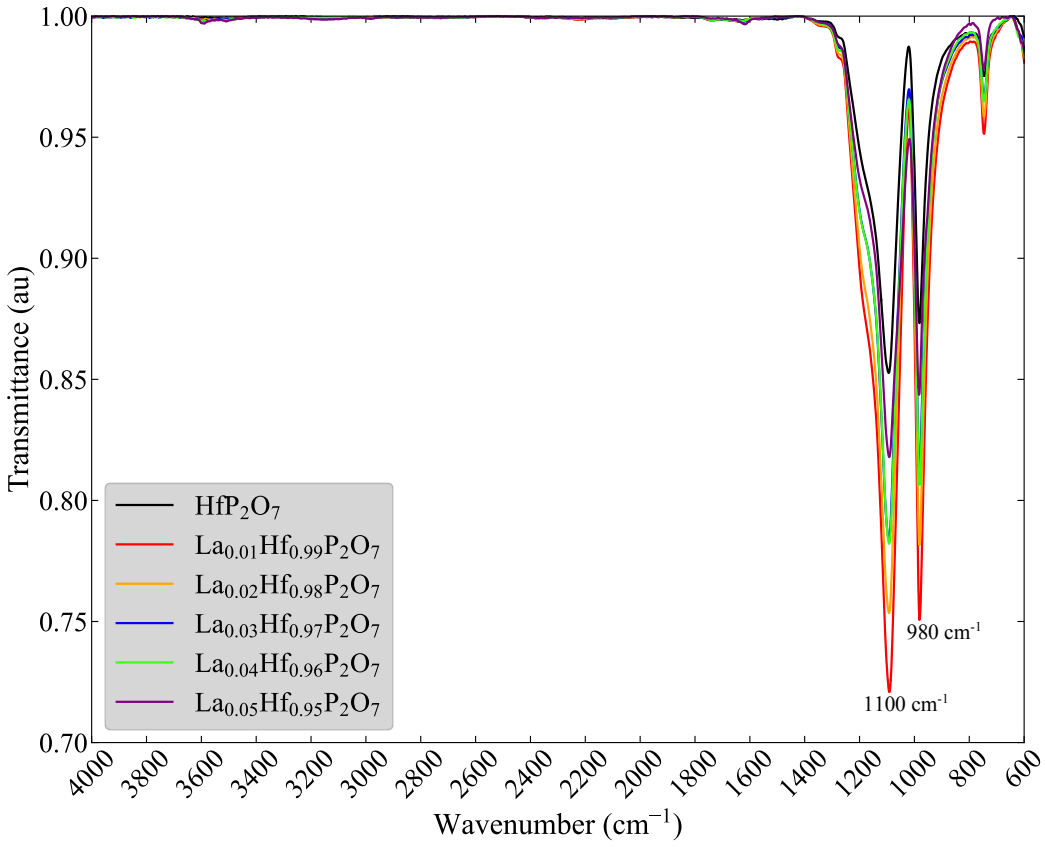

Figure 3.12: Group 2's FTIR spectra superimposed over one another.

Table 3.6: Group 2's FTIR characteristic signals and their corresponding functional group vibrations

Sample	Wavenumber (cm^{-1})		
	Peak 1	Peak 2	Peak 3
HfP_2O_7	1094,1	981,86	746,06
$La_{0.01}Hf_{0.99}P_2O_7$	1094,1	981,86	746,06
$La_{0.02}Hf_{0.98}P_2O_7$	1092,8	981,26	746,07
$La_{0.03}Hf_{0.97}P_2O_7$	1093,2	981,52	746,16
$La_{0.04}Hf_{0.96}P_2O_7$	1092,6	981,18	746,4
$La_{0.05}Hf_{0.95}P_2O_7$	1092,0	982,74	746,97

3.5 Transmission electron microscopy analysis (TEM)

To determine crystallite size and analyse the morphological features of the synthesized $La_xHf_{1-x}P_2O_7$, TEM images were collected on all the samples. TEM' was used to also determine the presence of any defects in the crystals [117], grain boundaries [118], and structural information [119] that could help explain certain physical properties exhibited by $La_xHf_{1-x}P_2O_7$ such as thermal integrity, ionic conductivity, and the degree of crystallinity.

Group 1's TEM images (Figure 3.13) confirmed the materials' amorphous nature, due to the absence of lattice fringes [119]. Lattice fringes are commonly found in crystalline materials as they are the visual representation of the d-spacing described by the space between two atomic planes in a crystal lattice [120]. While weak lattice fringes may imply weak coherence and weak contrast in the imaging process [119], no fringes are seen at all, hence the confirmation of amorphous nature of the materials in Group 1. This, therefore, complements the short-range order observed in Group 1's PDF data (Figure 3.7).

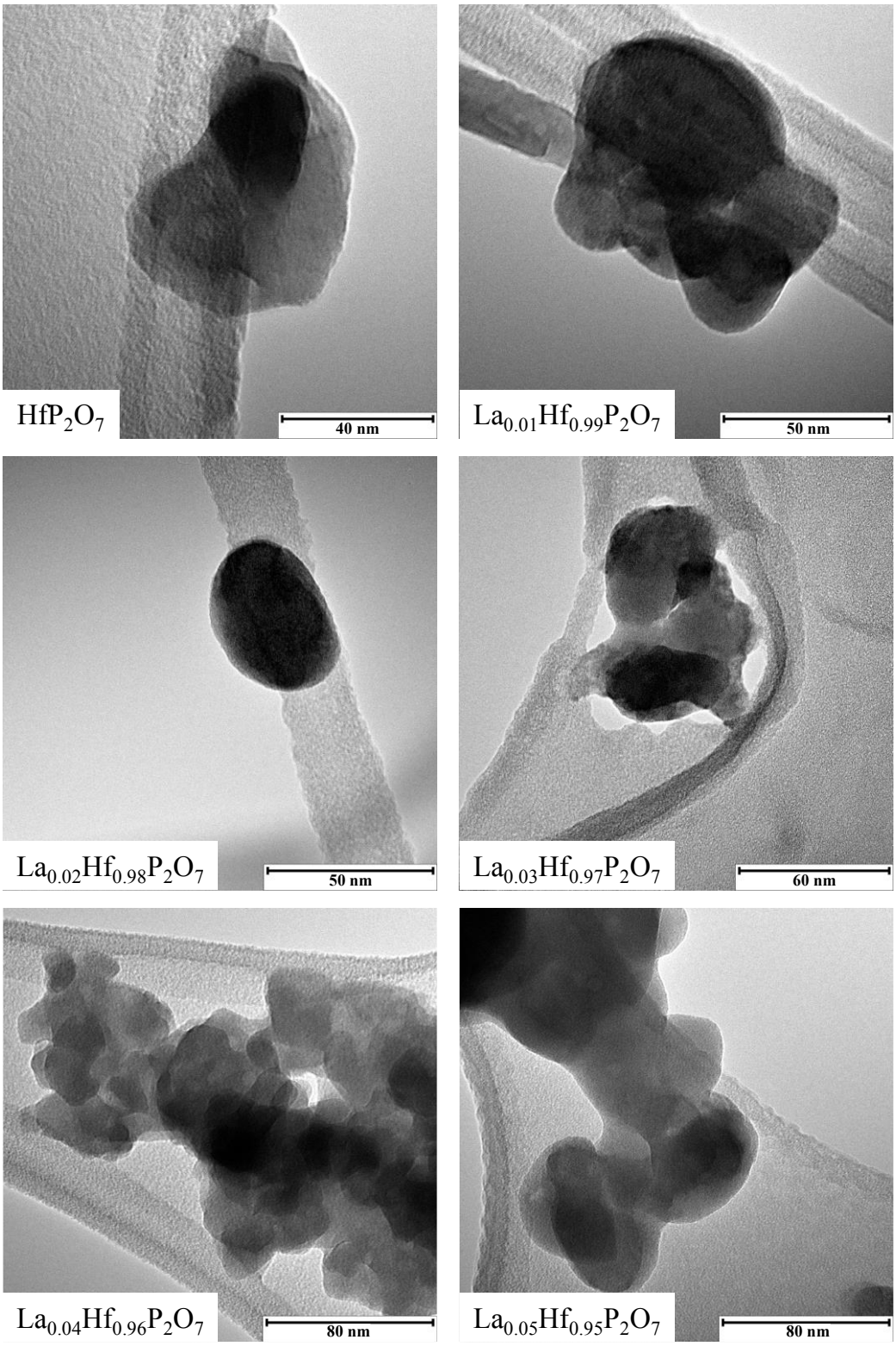

Figure 3.13: TEM images of Group 1's materials displaying the oval morphology of the particles, their small size, and their tendency to aggregate.

Group 1's particle size distribution (Figure 3.14) showed that the 20-30 nm size range dominated, suggesting a significant presence of particles within this specific size range. Moreover, no increasing nor decreasing trends in the particle size distributions with increasing La^{3+} concentrations were observed, therefore showing no contribution of size alterations by La^{3+} in the up to 5%.

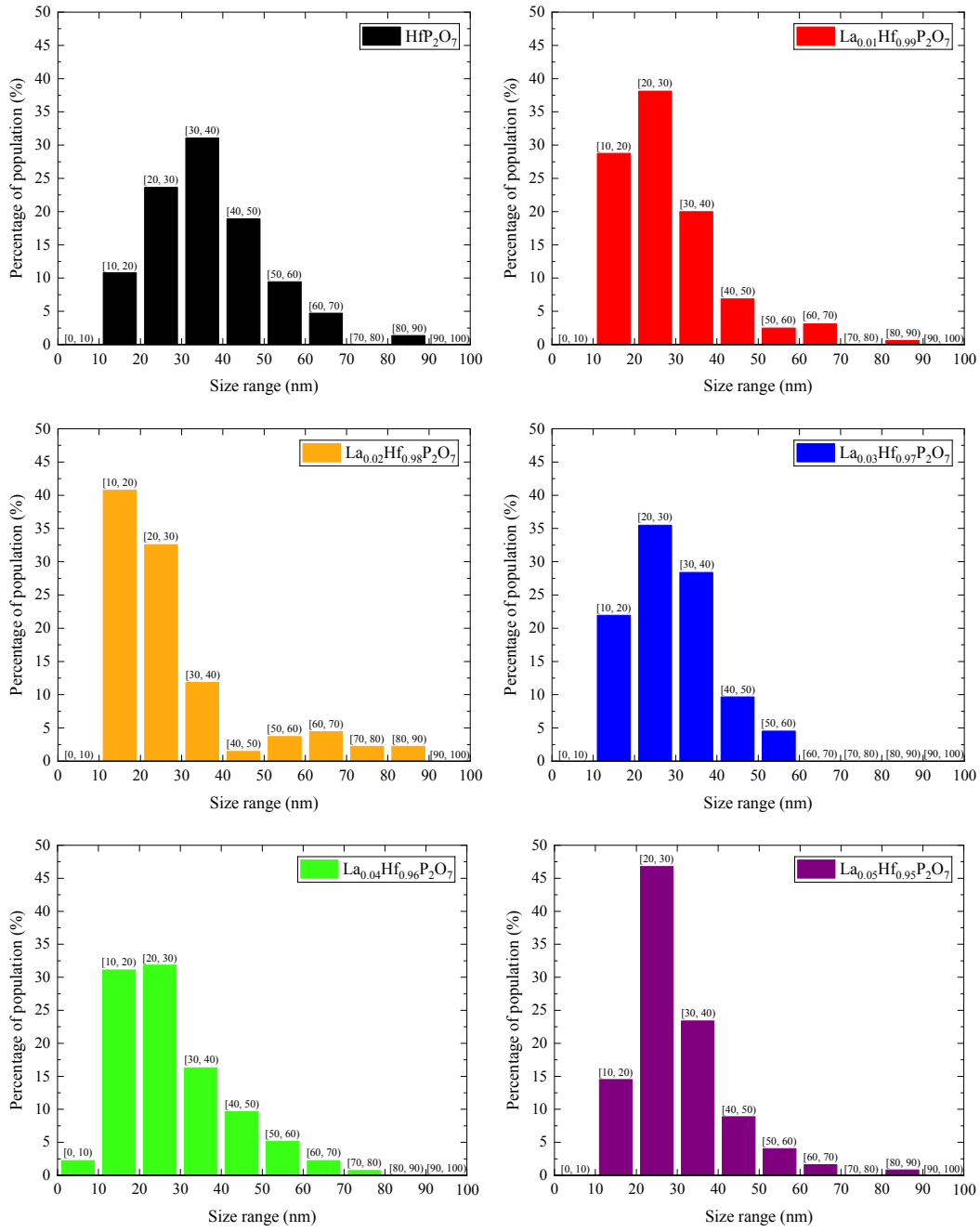

Figure 3.14: Percentage particle size distribution of Group 1's materials showing a tendency for most materials' particles' size to lie within the the 20-30 nm range.

The particles illustrated in Figure 3.14 were observed to adopt an oval shape, similar to that of zirconium pyrophosphate found by Chen et al. 2022 in their SEM images [121].

Group 2's TEM images (Figure 3.15) confirmed the opposite to that of Group 1's materials – the crystalline nature of the materials as substantiated by the presence of lattice fringes [119]. Group 2's PDF data (Figure 3.9) was, therefore, also complemented by its TEM data.

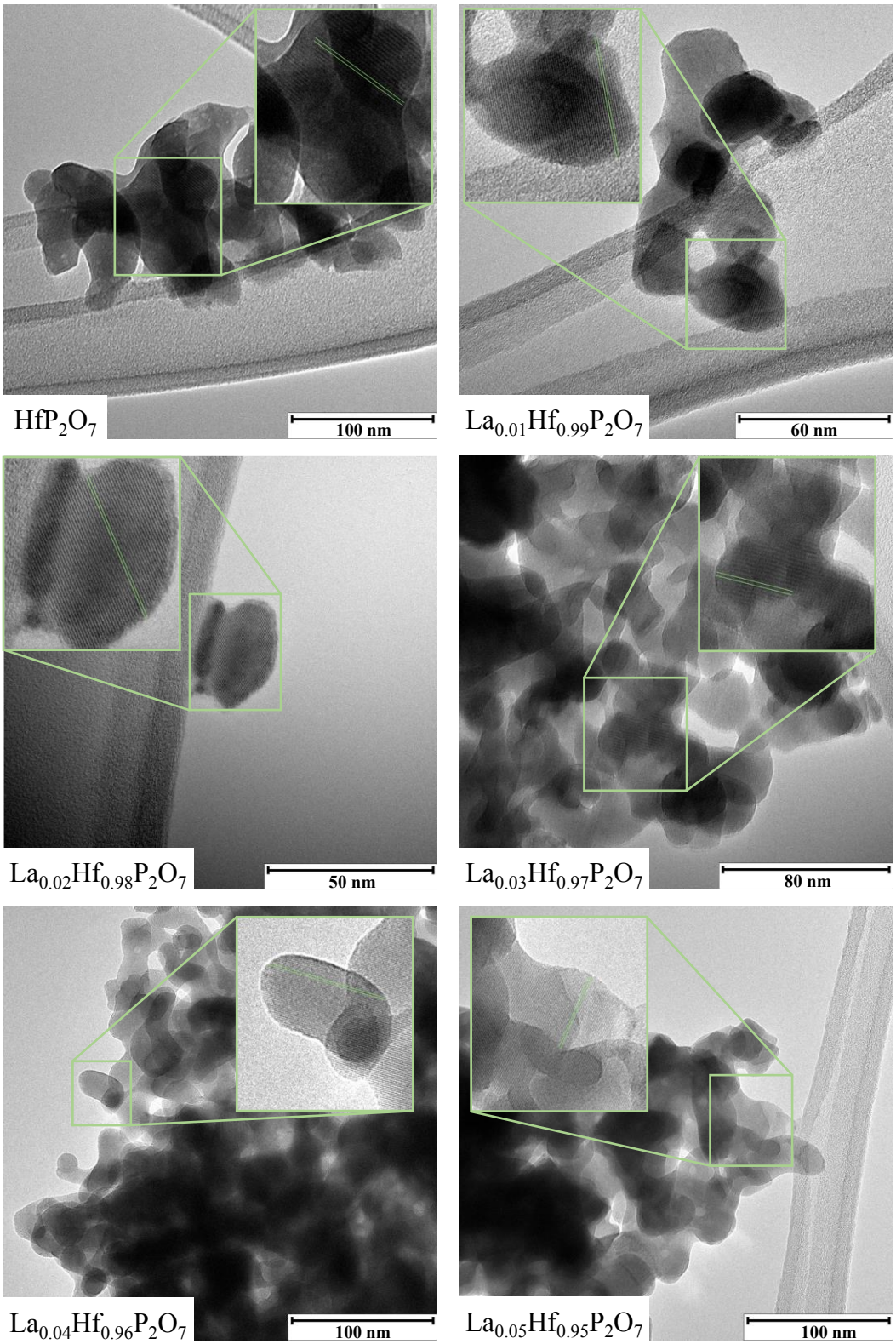

Figure 3.15: TEM images of Group 2's materials exhibiting lattice fringes (highlighted by green lines) commonly found in crystalline materials.

Group 2's particle size distribution (Figure 3.16) also showed that the 20-30 nm crystal size range dominated, which suggested a significant presence of particles within this specific size range, regardless of the degree of crystallinity in the materials. Moreover, no increasing nor decreasing trends in the particle size distributions with increasing La^{3+} concentrations were observed, therefore showing no contribution of size alterations by La^{3+} in the up to 5%.

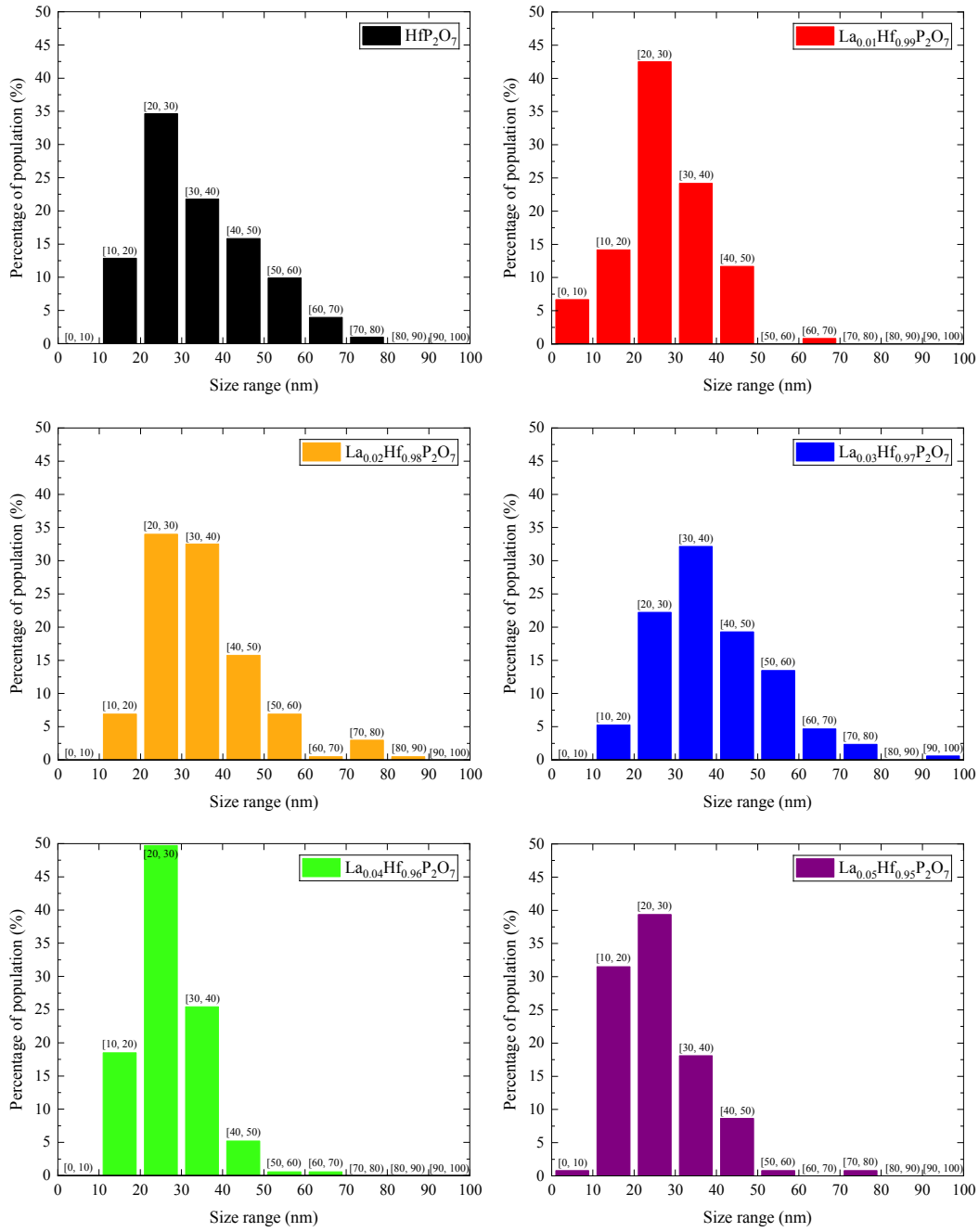

Figure 3.16: Percentage particle size distribution of Group 2's materials.

In addition to crystallite size, the crystallites in the TEM images were observed to adopt an oval shape, analogous to the particles of Group 1's materials.

While TEM provided visual insight into the particle features of the materials, the thermal integrity and ionic conductivity of both the amorphous and crystalline $La_xHf_{1-x}P_2O_7$ samples were then analysed.

Chapter 4: Physical Analysis

4.1 Simultaneous thermal analysis (STA – DTA/TGA)

STA is a thermal analysis technique that is used to determine temperature related changes to materials. These include glass transitions, crystallisation points, and melting points, to name a few [122]. These features present either as exothermic or endothermic signals, which point up or down on the spectrum, respectively (Figure 4.1).

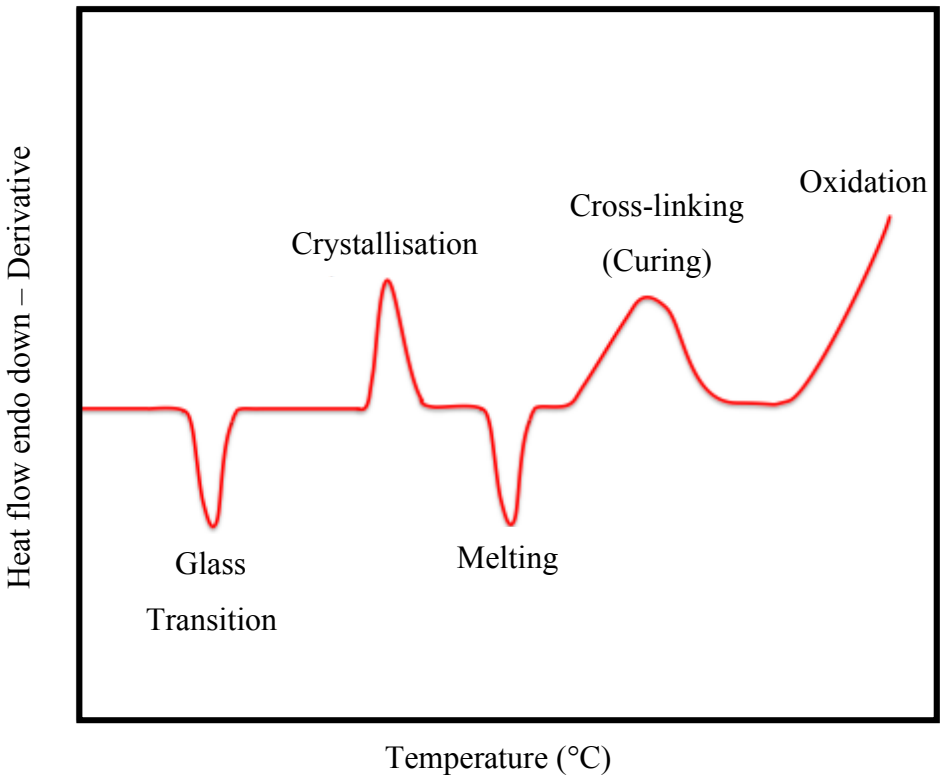

Figure 4.1: Illustration of a DTA curve showing different types of features that a material can exhibit and how they present on the curve [123].

There are several thermal events that can occur when performing an STA on a material that suggest which processes are occurring during the analysis (Table 4.1).

Table 4.1: Processes corresponding to thermal features in STA curves [122].

Process	TGA effect		DTA effect	
	Gain	Loss	Exothermic	Endothermic
Adsorption	✓		✓	
Desorption		✓		✓
Dehydration/desolvation		✓		✓
Sublimation		✓		✓
Vaporisation		✓		✓
Decomposition		✓	✓	✓
Solid-solid transition			✓	✓
Solid-gas reaction	✓	✓	✓	✓
Solid-solid reaction	Maybe	Maybe	✓	✓
Crystallisation			✓	
Melting				✓
Polymerisation		Maybe	✓	
Catalytic reactions	Maybe	Maybe	✓	

STA was performed on the samples to determine their thermal stability. Figure 4.2 shows the derivative of the heat flow and the percentage weight loss in Group 1's materials in the temperature range of 30 – 900 °C. A flat line was observed in all of Group 1's materials, therefore exhibiting no significant features. This indicated that all samples were able to withstand temperatures up to and including 900 °C without experiencing a phase change or any other significant thermal events. While there are subtle spikes in the DTA data, these were attributed to artifacts arising from the probable movement the crucible. Similarly, a near flat line was observed in the TGA, with only a ~2% weight loss observed, with the return of some mass when returning to 30 °C observed. This weight loss and regain was attributed to dehydration when heated to 900 °C, and rehydration when returning to 30 °C. Therefore, there is no evidence of thermal decomposition in the TGA nor thermal events in the DTA in this temperature range, which is incredibly meaningful for components in applications in high temperature operated energy devices. However, it must be noted that the temperatures were not sustained to determine whether the materials can withstand these temperatures for extended periods of time without changing.

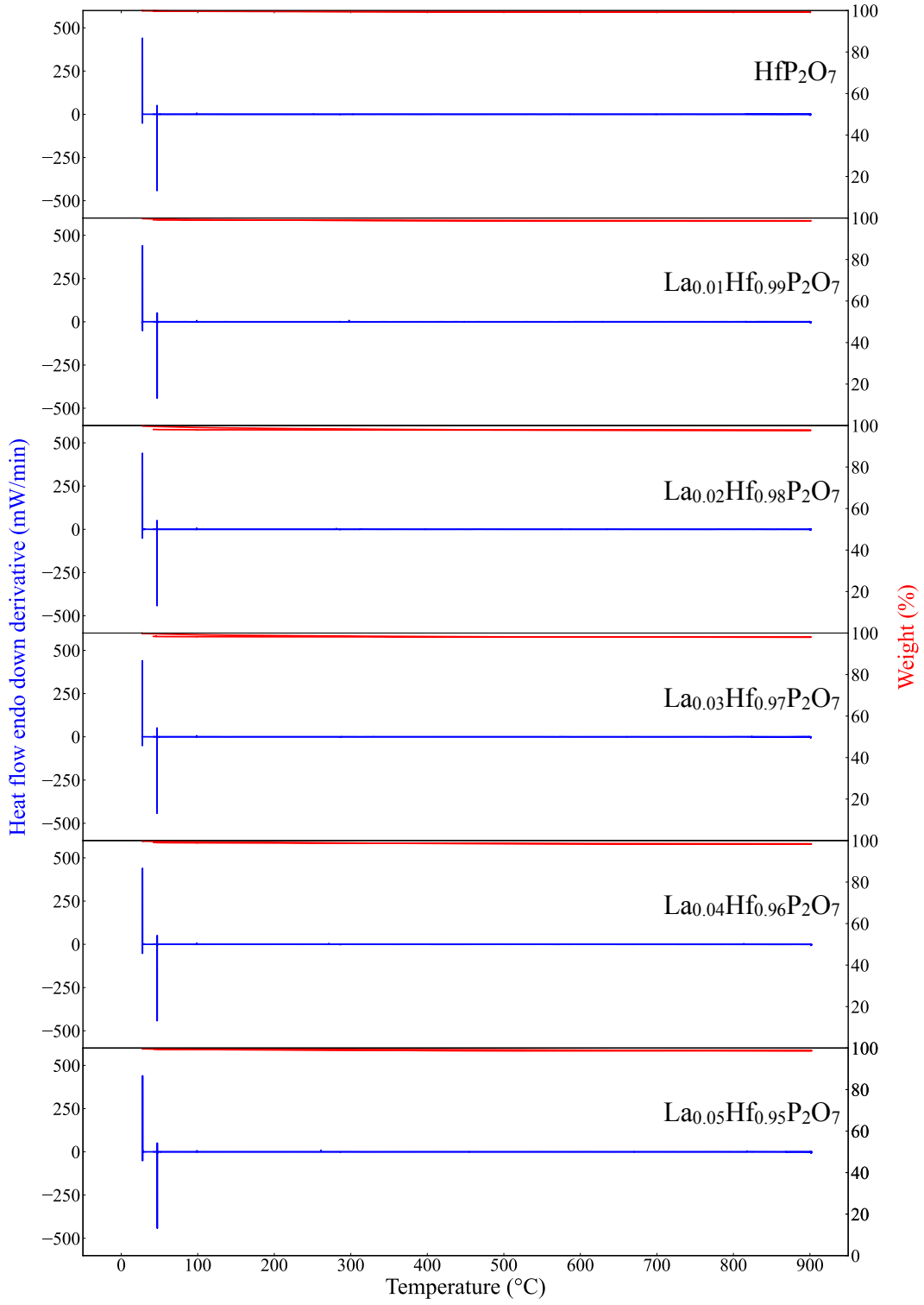

Figure 4.2: STA curves of Group 1's materials illustrating their simultaneous measurements of the DTA (blue) and TGA (red) analyses.

The same measurements were performed on Group 2's materials (Figure 4.3), and gave rise to similar results, exhibiting no significant differences. Therefore, both groups of materials show significant potential in high temperature applications.

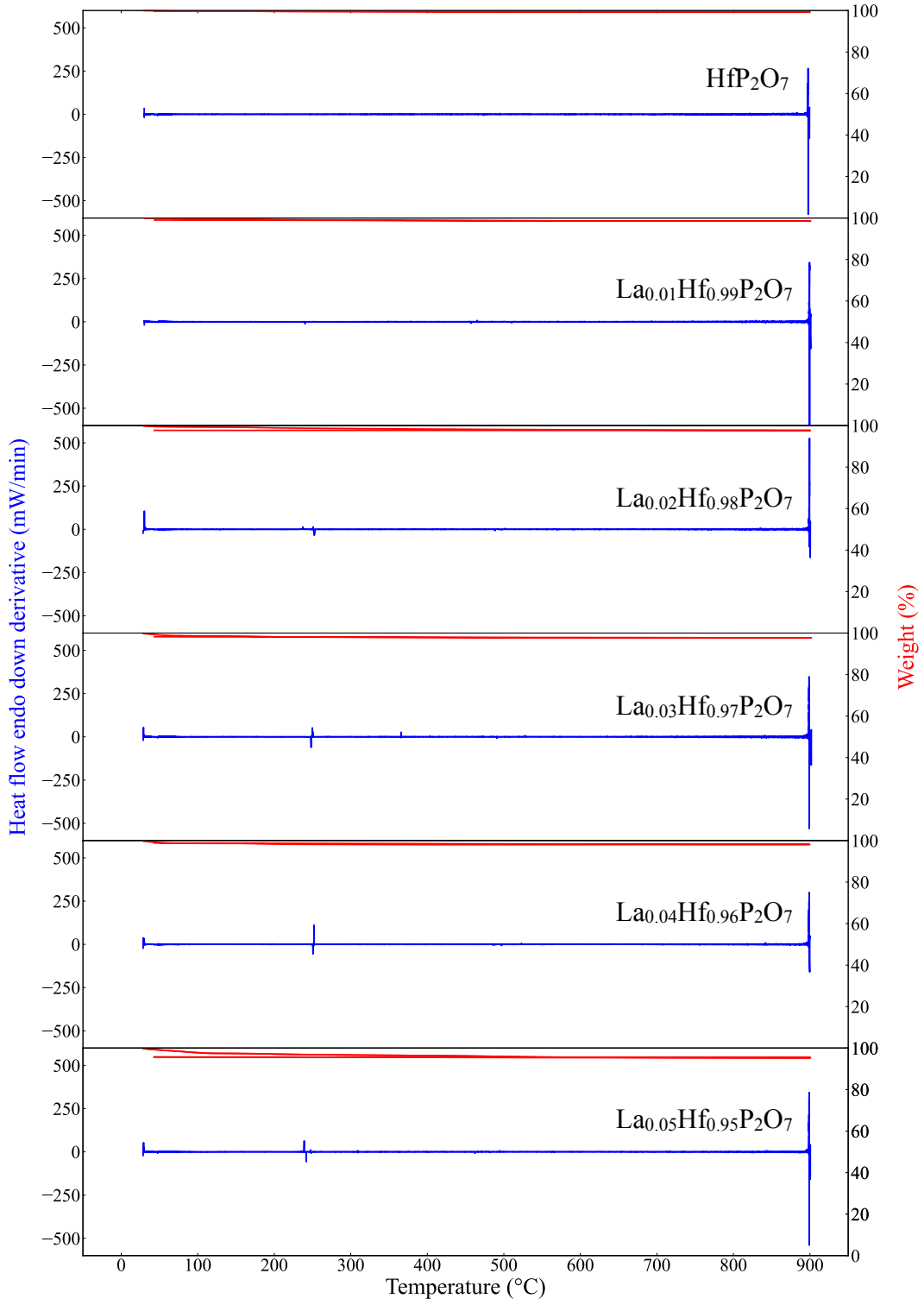

Figure 4.3: STA curves of Group 2's materials illustrating their simultaneous measurements of the DTA (blue) and TGA (red) analyses.

4.2 Potentiometric electrochemical impedance spectroscopy (PEIS)

Finally, after structural and thermal characterisation had been done, electrochemical properties of the samples were explored using PEIS [124]. This technique enabled us to study various electrochemical processes occurring at the electrode-electrolyte interface, as well as other potential interfaces such as those between grain boundaries [125].

PEIS measures the system's response to the applied potential enabling us to obtain data on the system's impedance properties [126]. By measuring the impedance response over a range of frequencies, PEIS provides insights into the charge transfer processes [127], double layer capacitance (C_{dl}) [128], and other electrochemical properties of $La_xHf_{1-x}P_2O_7$.

The impedance of the system is calculated based on the relationship between the applied potential, current response, and frequency. This impedance data is typically represented in Nyquist plots (Figure 4.4), where the real and imaginary parts of the impedance are plotted against each other to visualize the system's electrochemical behaviour.

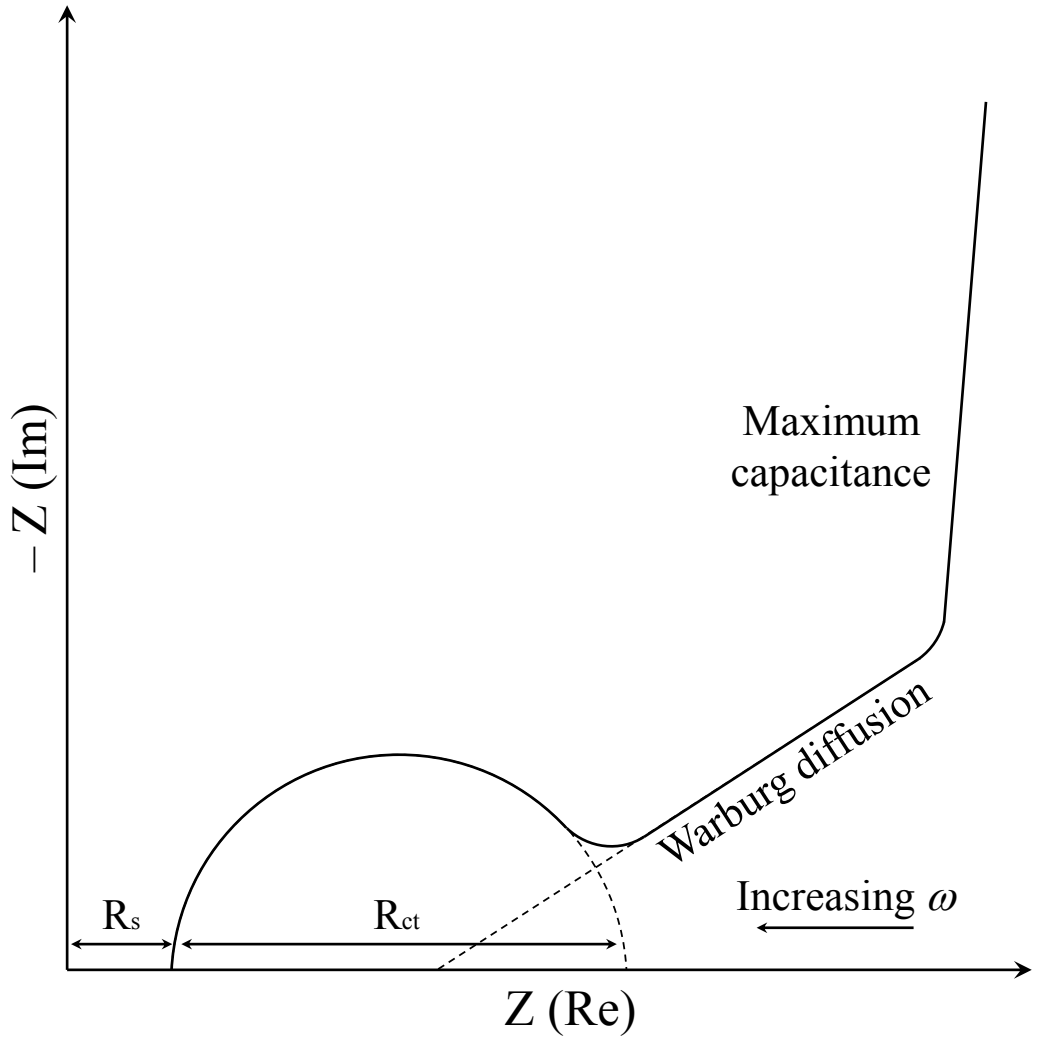

Figure 4.4: Schematic of typical Nyquist plots for EDLC systems [129] – R_s = Solution/Electrolyte Resistance; R_{ct} = charge transfer resistance; ω = frequency; Z (Re) = real impedance (resistance); –Z (Im) = imaginary impedance (capacitance).

In preparation for PEIS analysis of Group 1 and 2's materials, the samples were pressed into pellets, sintered and the dimensions measured for calculation of the ionic conductivities. These dimensions are shown in Table 4.2. The pellets were then coated with 10nm of gold on each face to ensure a good connection between the pellets and the electrodes.

Table 4.2: Dimensions of pellets after sintering.

Sample Name	Diameter (d) (cm)		Thickness (l) (cm)		Surface Area (S) (cm^2)	
	Group 1	Group 2	Group 1	Group 2	Group 1	Group 2
HfP_2O_7	0,808	0,810	0,144	0,142	0,5128	0,5153
$La_{0.01}Hf_{0.99}P_2O_7$	0,808	0,809	0,140	0,145	0,5128	0,5140
$La_{0.02}Hf_{0.98}P_2O_7$	0,808	0,809	0,154	0,144	0,5128	0,5140
$La_{0.03}Hf_{0.97}P_2O_7$	0,808	0,813	0,144	0,153	0,5128	0,5191
$La_{0.04}Hf_{0.96}P_2O_7$	0,814	0,808	0,152	0,148	0,5204	0,5128
$La_{0.05}Hf_{0.95}P_2O_7$	0,814	0,809	0,156	0,150	0,5204	0,5140

The surface area of the pellets' faces (Table 4.2) was calculated using the equation,

$$S = \pi \times \left(\frac{d}{2}\right)^2$$

The PEIS data recorded and fitted in EC-Lab for Group 1 was illustrated in Figure 4.6. The data suggested that there was no clear trend in the impedance, however, there was a major drop in impedance with the addition of La^{3+}. With regards to the Z-Fit of Group 1's HfP_2O_7, no realistic equivalent circuit model was found to provide a better fit, hence the seemingly bad Z-Fit of this data. To determine the conductivity from the Nyquist plots, equivalent circuit models (Figure 4.5) were fitted to the data.

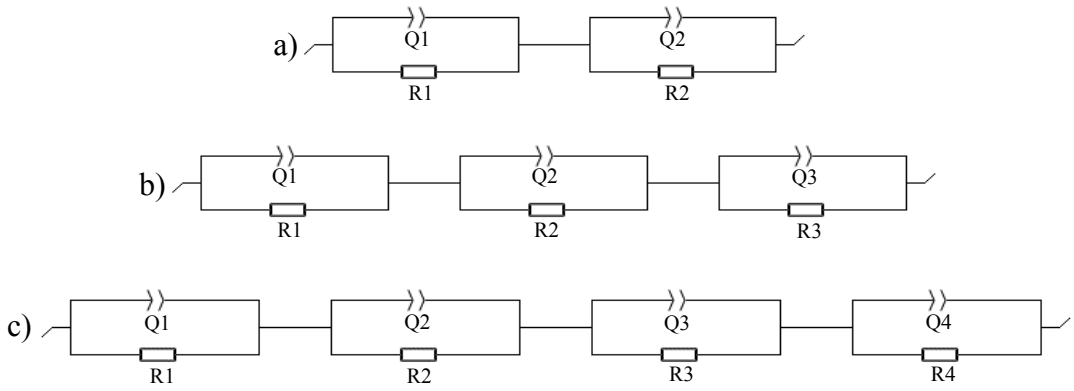

Figure 4.5: Equivalent circuit models fitted to Group 1 and 2's samples' PEIS data; a) fitted to all data with exceptions b) fitted to $La_{0.01}Hf_{0.99}P_2O_7$, and c) fitted to $La_{0.03}Hf_{0.97}P_2O_7$.

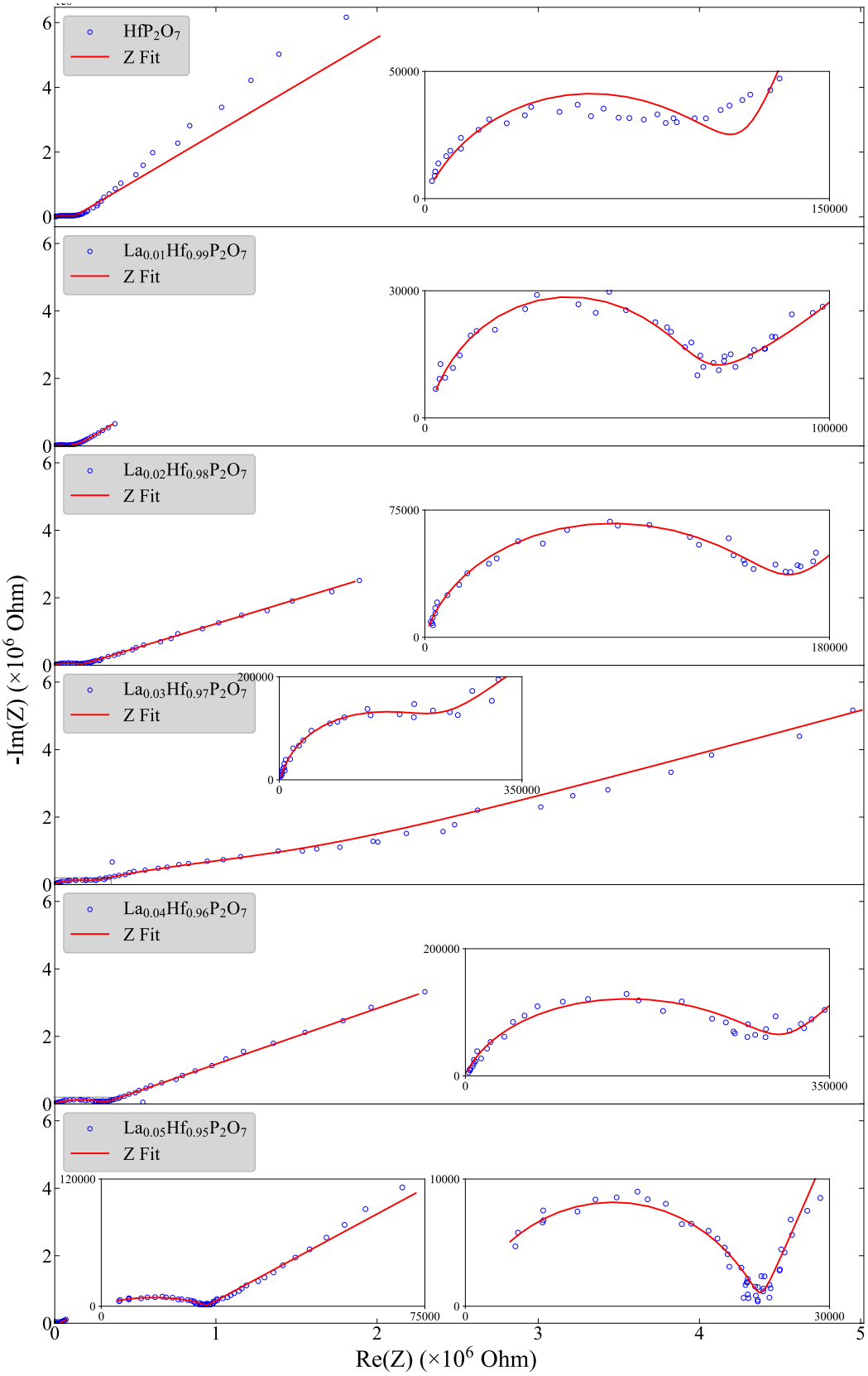

Figure 4.6: Nyquist plots of Group 1's samples obtained from room temperature PEIS with their equivalent circuit models fitted to their data, with magnified insets.

The resulting fits (Figure 4.6 and Figure 4.10) provide the values that each circuit component contributes to the impedance exhibited by the materials – Q is the constant phase element (CPE) which represents an interpolation between a capacitor and resistor, in place of the capacitance (C) and can be considered a pseudo-capacitive element – Figure 4.7 shows the deviation of Q from the ideal behaviour of C.

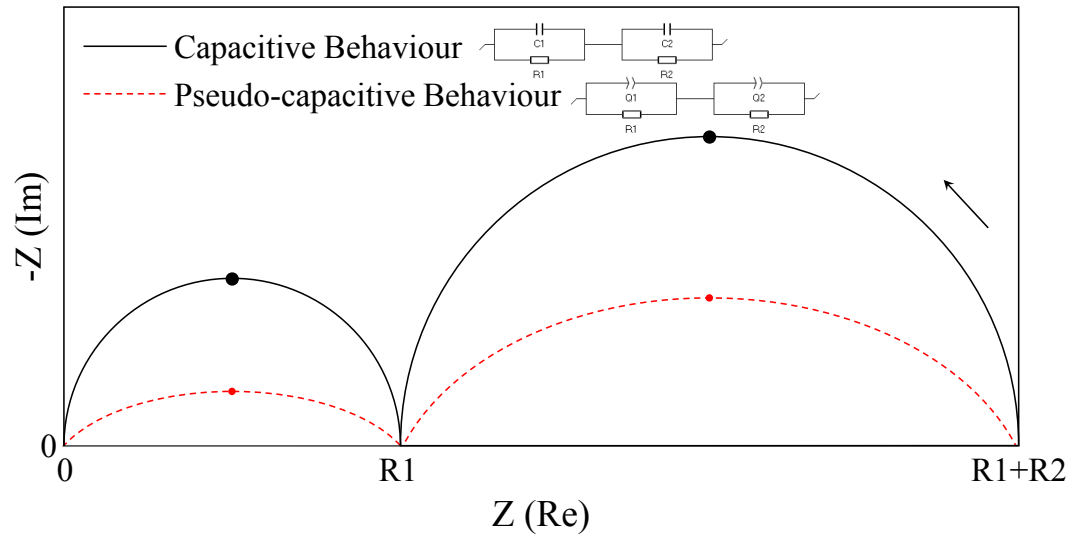

Figure 4.7: PEIS Nyquist plot simulations of the equivalent circuit models as depicted in the legend – ideal capacitive behaviour = –, pseudocapacitive behaviour deviating from ideal capacitive behaviour = ---.

These values were then used to calculate the overall ionic conductivity each material exhibits over a frequency range of 1 MHz to 1 kHz. When interpreting the PEIS of $La_xHf_{1-x}P_2O_7$, we saw that instead of exhibiting Warburg impedance as expected, there may be multiple charge transfer resistance components interfering with their preceding charge transfer components out of the scope of the frequency range. This may be a result of multiple interface types either within the material or the entire PEIS system giving rise to multiple interfaces within the material that charge carriers must be transported across.

From the resistance contributed by each component was used to calculate the ionic conductivities of each material and were plotted (Figure 4.8) for comparison.

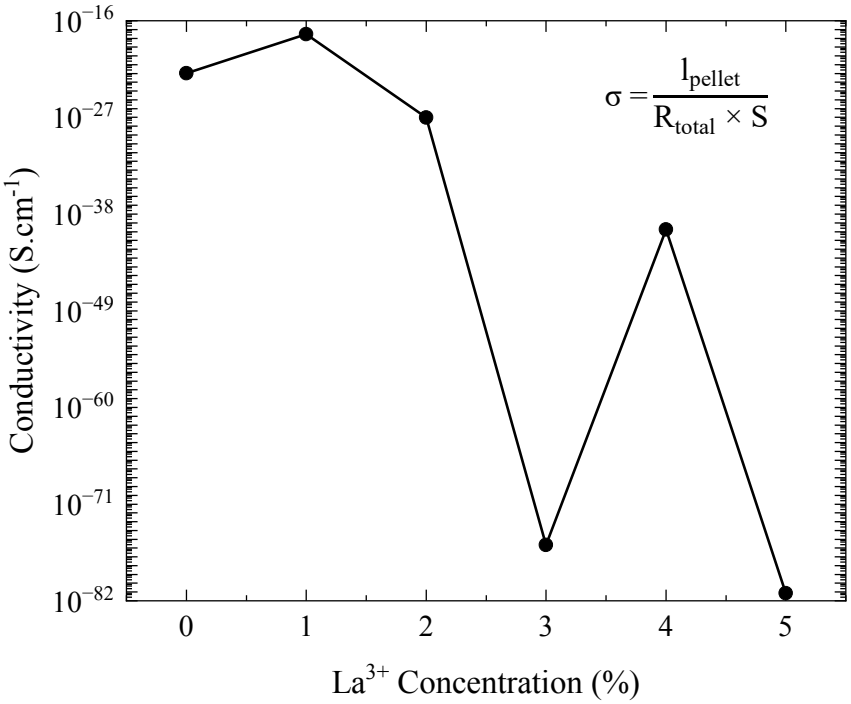

Figure 4.8: Logarithmic plot showing Group 1's change in room temperature conductivity (S.cm^{-1}) with increasing La^{3+} concentration; σ = conductivity; l_{pellet} = pellet thickness; R_{total} = sum of all components' resistance contributions.

Group 2's impedance spectra showed more of a trend with the exception of $La_{0.01}Hf_{0.99}P_2O_7$ which showed a lower impedance than expected in Group 2. This drop in impedance suggested that doping with La^{3+} in crystalline $La_xHf_{1-x}P_2O_7$ reduced the impedance experienced by the material with increasing concentration.

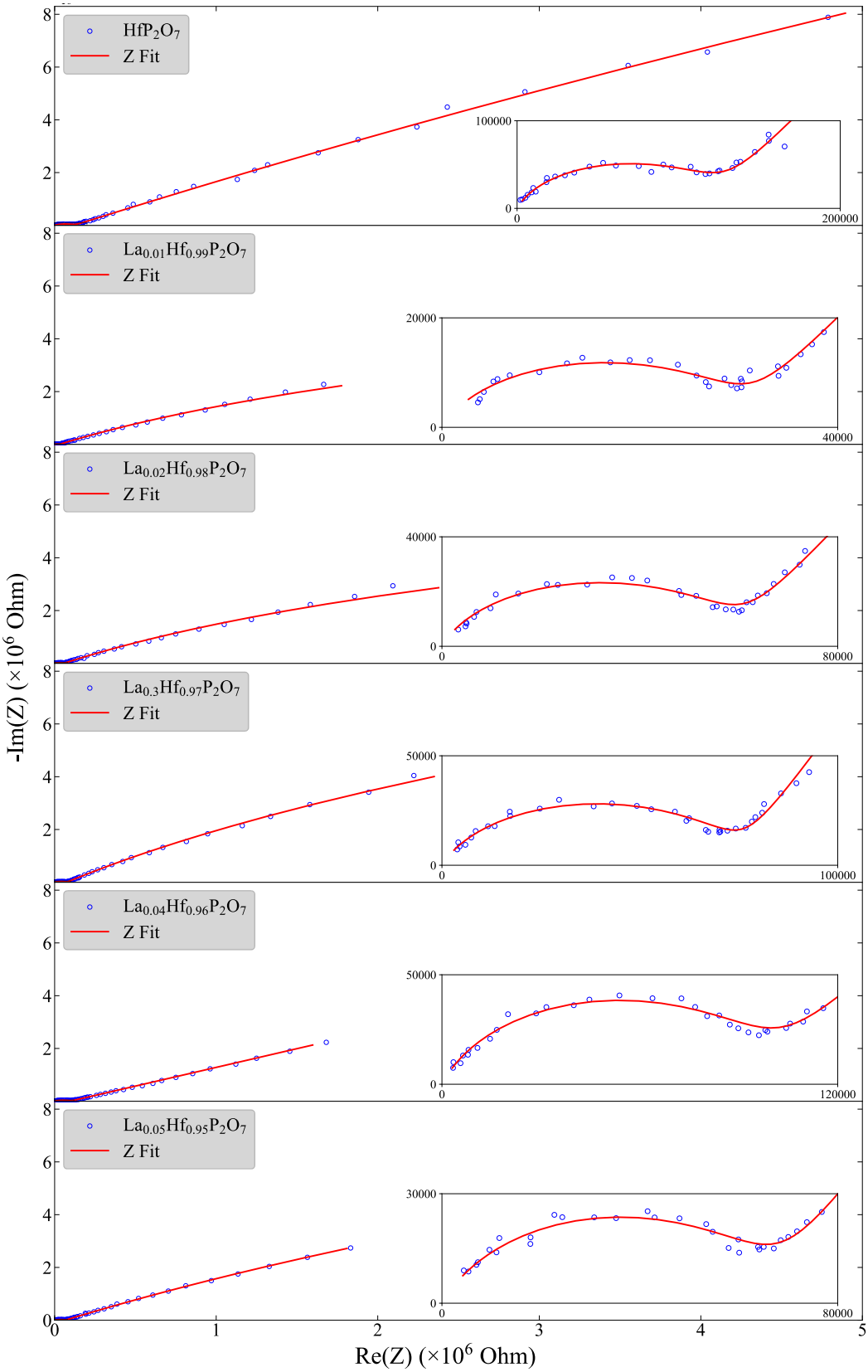

Figure 4.10: Nyquist plots of Group 2's samples obtained from room temperature PEIS with their equivalent circuit models fitted to their data, with magnified insets.

From this data, the conductivity was calculated using the values determined in EC-Lab from each sample's impedance spectrum and a line graph (Figure 4.11) showed how ionic conductivity changed with dopant concentration.

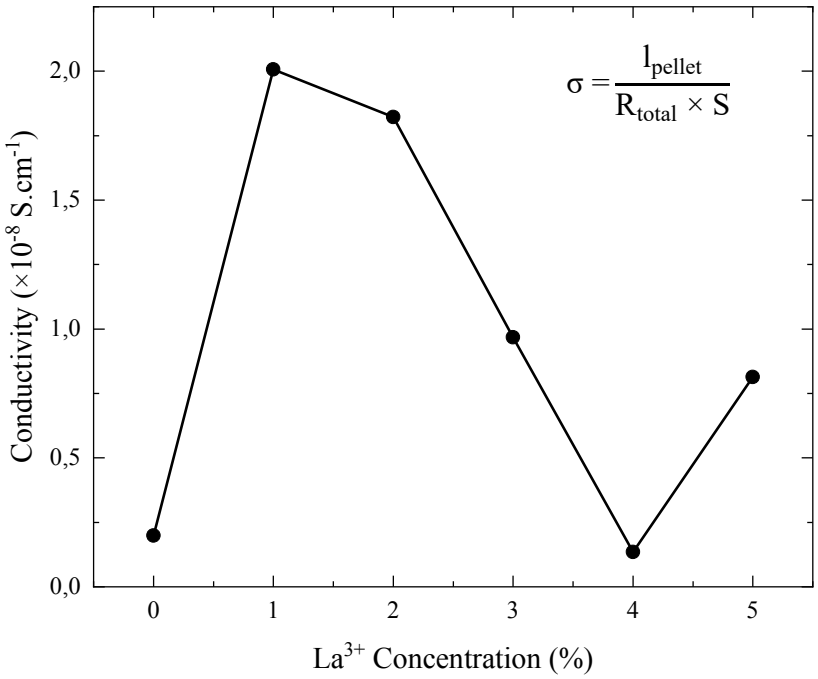

Figure 4.11: Line/scatter plot showing Group 2's change in room temperature conductivity (S.cm^{-1}) with increasing La^{3+} concentration; σ = conductivity; l_{pellet} = pellet thickness; R_{total} = sum of all components' resistance contributions.

Figure 4.11 showed no trend in the ionic conductivity values; this does not, however, mean that there would not be a trend of the samples' conductivities at varying temperatures. Jin et al., 2010 showed in Figure 4.12 that at certain varying temperatures, an increasing conductivity with an increasing amount of dopant present in the samples [50] and an increase in conductivity across all samples with increasing temperature.

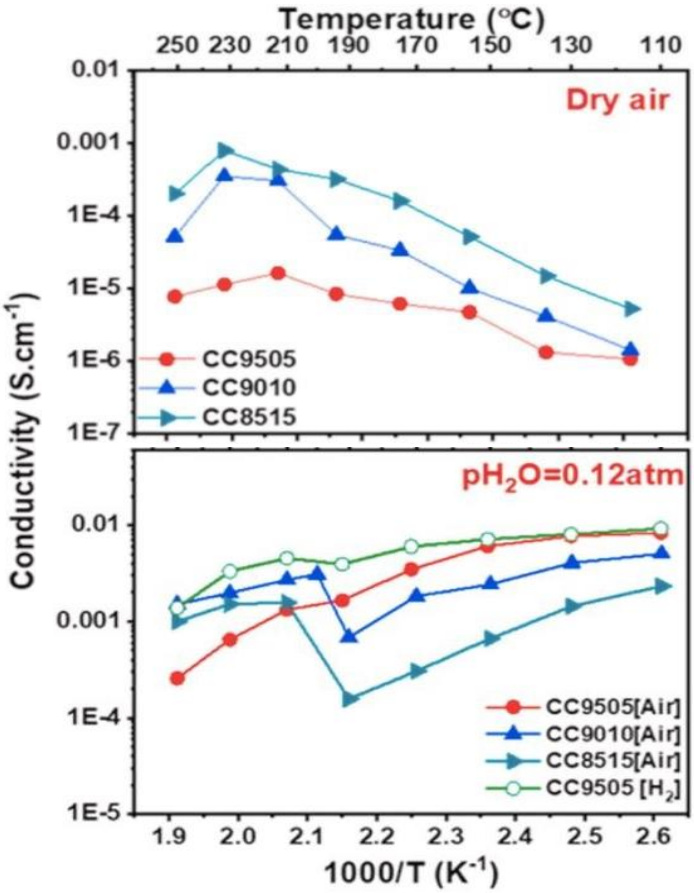

Figure 4.12: Variation of ionic conductivity of $Gd_{0.1}Ce_{0.9}P_2O_7$ combined with penta-hydrogen diphosphate in the range of 5 – 15% by weight under (a) dry conditions in air and (b) humidified air [50].

Therefore, both groups of $La_xHf_{1-x}P_2O_7$ must be studied further at varying temperatures to find the optimum ionic conductivity temperature of the materials using variable temperature PEIS for a more comprehensive understanding of the materials.

Conclusions

The comprehensive characterization of the $La_xHf_{1-x}P_2O_7$ materials synthesized in this study via two variants of the sol-gel technique, denoted group 1 and 2, respectively, has provided valuable insights into their structural and functional properties. Through a combination of various characterisation techniques, including PXRD, ^{31}P MAS ssNMR, PDF, FTIR, TEM, STA, and PEIS, a detailed understanding of the materials' composition, structure, and physical properties was attained.

The PXRD data clearly indicated that Group 1's materials were amorphous, while Group 2's materials exhibited crystalline behaviour. A structure model with the orthorhombic space group, *Pbca*, was successfully fitted to Group 2's PXRD data, with an average GoF of 1.95 and R_{wp} of 6.645 indicating satisfactory fits. The introduction of La^{3+} increased the GoF value only slightly, however, the 5% doped phase showed a much greater increase in the GoF value signifying that this concentration of La^{3+} starts affecting the structure of the phase. The ^{31}P MAS ssNMR data revealed distinct phosphorous signals for both groups, highlighting the different P environments in the $La_xHf_{1-x}P_2O_7$ samples. It was found that increasing the La^{3+} concentration in both Group 1 and 2's samples gave rise to an increasing intensity of the –5 ppm signal.

The PDF data provided insights into the short-range order of Group 1's materials, while Group 2's PDF data was refined using the same structure model as in PXRD refinements, showing a good fit. Group 2's PDF data was then used for the qualitative interpretation of Group 1's PDF data due to the lack of a suitable structure model that could fit to its narrow atomic distance range. The comparison of Group 1 and 2's PDF data showed similarities in the range of 0 – 5.5 nm, confirming their local structure a match. There were no significant changes with the addition of La^{3+} in the doping range used which suggested which suggested a homogeneous distribution of the dopants and was also anticipated due to the similar sized cation (Hf^{4+}) it was replacing.

The FTIR spectra of both groups exhibited similarities in the significant signals corresponding to the P-O-P moiety, with the asymmetric and symmetric P-O stretches in the P-O-P moiety corresponding to the strong signals at ~1000cm^{-1} and ~900cm^{-1}, respectively, confirming the presence of the pyrophosphate functional group. The addition of La^{3+} showed no significant changes due to the low dopant concentrations used.

TEM images confirmed the amorphous nature of Group 1's materials and the crystallinity of Group 2's materials, with particle size distributions revealing dominant particle sizes in the 20-30 nm range for both groups. The crystallites were observed to be oval in shape and showed evidence of aggregation of the crystallites. While addition of La^{3+} did not show much evidence of change, the difference between sample sets group 1 and 2 was significant.

The STA data showed that the materials in both Group 1 and 2 demonstrated excellent thermal stability in both materials determined by the absence of any thermal events between 30 and 900 °C. Moreover, adding La^{3+} did not affect the thermal stability in the concentration range it was doped, making it good choice of dopant in terms of stability. This is a crucial leap forward in high-temperature energy applications.

PEIS data indicated a significant drop in impedance upon doping with La^{3+}, suggesting improved ionic conductivity with the addition of La^{3+}. However, no clear trend in the reduction of impedance with varying dopant concentrations was observed, therefore demanding further electrochemical studies.

Finally, not only were the materials characterised for potential energy storage and conversion applications, but the distinct synthetic procedures employed in the preparation of materials for Group 1 and Group 2 led to the formation of materials with different morphologies.

Group 1's method, which included a filtering step to eliminate excess solvent before calcination, likely contributed to the production of amorphous materials, as indicated by the absence of lattice fringes in the TEM images (Figure 3.13), the

short-range order observed in the PDF data (Figure 3.7) and the absence diffraction peaks observed in the PXRD data (Figure 3.1).

Group 2's approach, involving solvent removal via evaporation in air before calcination instead of filtering, resulted in the crystalline nature of the materials, evident from the presence of lattice fringes in the samples, the long-range order observed in the PDF data (Figure 3.9) and the presence of sharp diffraction peaks observed in the PXRD data (Figure 3.2). These differences underscore how subtle variations in synthetic procedures can significantly impact the structural properties and characteristics of the final materials, highlighting the importance of precision in controlling synthesis parameters in materials science.

Future Work

In future studies, the focus will be on synthesising and characterising analogous $Sc_xTi_{1-x}P_2O_7$ and $Y_xZr_{1-x}P_2O_7$ series of compounds. This would involve conducting a detailed structural analysis of all three metal pyrophosphates (including $La_xHf_{1-x}P_2O_7$), to determine the impact of dopant inclusion on their behaviour.

A structural analysis will be done by examining the crystal structures of the compounds to identify any deviations from expected behaviour, analogous to that in this study. By comparing the structural features of $Sc_xTi_{1-x}P_2O_7$ and $Y_xZr_{1-x}P_2O_7$ and the undoped compounds, insights can be gained into how dopants influence the material properties.

Utilising SEM analysis will allow for the observation of larger features and crystal morphology within the synthesized compounds. This detailed examination will provide valuable information on the microstructure of the materials, aiding in understanding their properties and potential applications.

Ensuring reproducibility is crucial in scientific research. Therefore, repeating the synthesis of the compounds multiple times will help validate the results obtained and confirm the consistency of the materials' properties. It will also validate the use of different synthetic methods for different morphological outcomes, and other properties, akin to this study where two variations of the sol-gel method resulted in an amorphous phase and a crystalline phase.

Conducting aging studies on the materials will provide insights into their long-term stability and performance. By monitoring changes in properties over time, it will be possible to assess the durability and reliability of the synthesized compounds.

To evaluate the practical feasibility of the materials, assessing them in novel capacitor and supercapacitor devices will be essential. This will determine their functional range and suitability for real energy applications, providing valuable information on their performance in practical settings.

By addressing these future research directions, a comprehensive understanding of the synthesised compounds' properties and potential applications can be achieved, contributing to advancements in materials science and energy storage technologies.

References

[1] T. Hibino, K. Kobayashi, M. Nagao, and S. Kawasaki, "High-temperature supercapacitor with a proton-conducting metal pyrophosphate electrolyte," *Sci Rep*, vol. 5, no. 1, p. 7903, 2015.

[2] David Segal, *Chemical synthesis of advanced ceramic materials*, vol. 1. Cambridge: Cambridge University Press, 1989.

[3] Preciseceramic.com, "Advanced Ceramics: Background, Types, and Applications." Accessed: Mar. 11, 2024. [Online]. Available: https://www.preciseceramic.com/blog/advanced-ceramics-background-types-and-applications.html

[4] J. Kelly and I. Denry, "Stabilized zirconia as a structural ceramic: An overview☆," *Dental Materials*, vol. 24, no. 3, pp. 289–298, Mar. 2008, doi: 10.1016/j.dental.2007.05.005.

[5] M. A. Anderson, M. J. Gieselmann, and Q. Xu, "Titania and alumina ceramic membranes," *J Memb Sci*, vol. 39, no. 3, pp. 243–258, Dec. 1988, doi: 10.1016/S0376-7388(00)80932-1.

[6] G. Petzow and M. Herrmann, "Silicon Nitride Ceramics," 2002, pp. 47–167. doi: 10.1007/3-540-45623-6_2.

[7] F. Chen, Q. Shen, J. M. Schoenung, and L. Zhang, "Synthesis and Pressureless Sintering of Zirconium Phosphate Ceramics," *Journal of the American Ceramic Society*, vol. 91, no. 10, pp. 3173–3180, Oct. 2008, doi: 10.1111/j.1551-2916.2008.02610.x.

[8] L. Perera, L. Palliyaguru, L. D. Dhanushka, C. D. Jayaweera, R. K. Dulanjalee, and P. M. Jayaweera, "A novel route to synthesize metal titanium phosphate ceramic pigments: Co, Ni, and Cu-incorporated α-Ti(HPO4)2·H2O from ilmenite," *Ceram Int*, vol. 48, no. 16, pp. 22906–22916, Aug. 2022, doi: 10.1016/j.ceramint.2022.04.246.

[9] P. K. Jha, O. P. Pandey, and K. Singh, "FTIR spectral analysis and mechanical properties of sodium phosphate glass–ceramics," *J Mol Struct*, vol. 1083, pp. 278–285, Mar. 2015, doi: 10.1016/j.molstruc.2014.11.027.

[10] C. B. Carter and M. G. Norton, *Ceramic Materials: Science and Engineering*, Second. New York, NY: Springer. doi: https://doi.org/10.1007/978-1-4614-3523-5.

[11] B. Singh *et al.*, "Fast ionic conduction in tetravalent metal pyrophosphate-alkali carbonate composites: New potential electrolytes for intermediate-temperature fuel cells," *J Power Sources*, vol. 345, pp. 176–181, Mar. 2017, doi: 10.1016/j.jpowsour.2017.02.006.

[12] B. Singh, H.-N. Im, J.-Y. Park, and S.-J. Song, "Studies on Ionic Conductivity of Sr^{2+} -Doped CeP_2O_7 Electrolyte in Humid Atmosphere," *The Journal of Physical Chemistry C*, vol. 117, no. 6, pp. 2653–2661, Feb. 2013, doi: 10.1021/jp311547g.

[13] Madhu, "What is the Difference Between Inorganic Phosphate (Pi) and Pyrophosphate (PPi)." Accessed: Jun. 13, 2023. [Online]. Available: https://www.differencebetween.com/what-is-the-difference-between-inorganic-phosphate-pi-and-pyrophosphate-ppi/

[14] M. Kawabe, O. Ohashi, and I. Yamaguchi, "Phosphorus nuclear magnetic resonance in polyphosphates and determination of their hydrolysis rate constants," *Bull Chem Soc Jpn*, vol. 43, no. 12, pp. 3705–3710, 1970.

[15] M. R. Hamczyk and R. Villa-Bellosta, "Pyrophosphate metabolism and calcification.," Dec. 2018, *United States*. doi: 10.18632/aging.101703.

[16] R. S. Levine, "Pyrophosphates in toothpaste: a retrospective and reappraisal," *Br Dent J*, vol. 229, no. 10, pp. 687–689, 2020.

[17] NEWSEED, "Application and Uses of Tetrasodium Pyrophosphate." Accessed: Jun. 13, 2023. [Online]. Available: https://www.foodsweeteners.com/applications-and-uses-of-tetrasodium-pyrophosphate/

[18] Persistance Market Research, "Sodium Acid Pyrophosphate Market." Accessed: Jun. 12, 2023. [Online]. Available: https://www.persistencemarketresearch.com/market-research/sodium-acid-pyrophosphate-market.asp#:~:text=Sodium acid pyrophosphate%2C often abbreviated,for meat and fish processing

[19] N. R. Council, "Water Chemicals Codex," 1982.

[20] Annabelle R Baker, “Synthesis and characterisation of novel metal pyrophosphates,” University of Birmingham, 2014.

[21] A. G. Meguerdichian *et al.*, “Synthesis and Electrocatalytic Activity of Ammonium Nickel Phosphate, $[NH_4]NiPO_4 \cdot 6H_2O$, and β-Nickel Pyrophosphate, $\beta\text{-}Ni_2P_2O_7$: Catalysts for Electrocatalytic Decomposition of Urea,” *Inorg Chem*, vol. 57, no. 4, pp. 1815–1823, Feb. 2018, doi: 10.1021/acs.inorgchem.7b02658.

[22] P. D. Solanki *et al.*, “Nickel Pyrophosphate Nanoparticles: Synthesis, Structural, Thermal, Spectroscopic, and Dielectric Studies,” *Nano*, vol. 17, no. 07, Jun. 2022, doi: 10.1142/S1793292022500497.

[23] Y. X. Ooi *et al.*, “Incorporation of titanium pyrophosphate in polybenzimidazole membrane for medium temperature dry PEFC application,” *Solid State Ion*, vol. 344, p. 115140, Jan. 2020, doi: 10.1016/j.ssi.2019.115140.

[24] T. Yang *et al.*, “$MH_2P_2O_7$ (M = Co, Ni): Metamagnetic Interaction between the Zigzag Octahedral Chains,” *Inorg Chem*, vol. 46, no. 7, pp. 2342–2344, Apr. 2007, doi: 10.1021/ic061665q.

[25] P. Senguttuvan, G. Rousse, J. Oró-Solé, J. M. Tarascon, and M. R. Palacín, “A low temperature TiP2O7 polymorph exhibiting reversible insertion of lithium and sodium ions,” *J Mater Chem A Mater*, vol. 1, no. 48, p. 15284, 2013, doi: 10.1039/c3ta13756b.

[26] L.-O. Hagman *et al.*, “Note on the Structures of MIV P2O7 (MIV = Ge, Zr, and U).,” *Acta Chem Scand*, vol. 23, pp. 327–328, 1969, doi: 10.3891/acta.chem.scand.23-0327.

[27] C.-H. Huang, O. Knop, D. A. Othen, F. W. D. Woodhams, and R. A. Howie, “Pyrophosphates of Tetravalent Elements and a Mössbauer Study of SnP_2O_7,” *Can J Chem*, vol. 53, no. 1, pp. 79–91, Jan. 1975, doi: 10.1139/v75-011.

[28] G. W. Stinton, M. R. Hampson, and J. S. O. Evans, “The 136-Atom Structure of ZrP_2O_7 and HfP_2O_7 from Powder Diffraction Data,” *Inorg Chem*, vol. 45, no. 11, pp. 4352–4358, May 2006, doi: 10.1021/ic060016b.

[29] J. Zemann, "*Crystal structures,* 2 *nd edition, Vol. 3* by R. W. G. Wyckoff," *Acta Crystallogr*, vol. 21, no. 3, pp. 455–455, Sep. 1966, doi: 10.1107/S0365110X6600327X.

[30] P. Senguttuvan, G. Rousse, J. Oró-Solé, J. M. Tarascon, and M. R. Palacín, "A low temperature TiP 2 O 7 polymorph exhibiting reversible insertion of lithium and sodium ions," *J Mater Chem A Mater*, vol. 1, no. 48, pp. 15284–15291, 2013.

[31] R. M. P. Colodrero, P. Olivera-Pastor, A. Cabeza, and M. Bazaga-García, "Properties and Applications of Metal Phosphates and Pyrophosphates as Proton Conductors," *Materials*, vol. 15, no. 4, p. 1292, Feb. 2022, doi: 10.3390/ma15041292.

[32] M. Ohara *et al.*, "A vanadium-based oxide-phosphate-pyrophosphate framework as a 4 V electrode material for K-ion batteries," *Chem Sci*, vol. 12, no. 37, pp. 12383–12390, 2021, doi: 10.1039/D1SC03725K.

[33] C. N. R. Rao, Srinivasan Natarajan, Amitava Choudhury, S. Neeraj, and A. A. Ayi, "Aufbau Principle of Complex Open-Framework Structures of Metal Phosphates with Different Dimensionalities," vol. 34, no. 1, 2001.

[34] Y. Niu, Y. Zhang, and M. Xu, "A review on pyrophosphate framework cathode materials for sodium-ion batteries," *J Mater Chem A Mater*, vol. 7, no. 25, pp. 15006–15025, 2019, doi: 10.1039/C9TA04274A.

[35] R. Murugavel, A. Choudhury, M. G. Walawalkar, R. Pothiraja, and C. N. R. Rao, "Metal Complexes of Organophosphate Esters and Open-Framework Metal Phosphates: Synthesis, Structure, Transformations, and Applications," *Chem Rev*, vol. 108, no. 9, pp. 3549–3655, Sep. 2008, doi: 10.1021/cr000119q.

[36] S. S. Patil and P. S. Patil, "Transition metal pyrophosphate (MxP2O7): A new arrival in hybrid supercapacitors," *Chemical Engineering Journal*, vol. 455, p. 140639, Jan. 2023, doi: 10.1016/j.cej.2022.140639.

[37] G. Alberti, M. Casciola, U. Costantino, A. Peraio, and T. Rega, "Proton-conducting solid dispersions of silica and zirconium phosphate pyrophosphate," *J Mater Chem*, vol. 5, no. 11, p. 1809, 1995, doi: 10.1039/jm9950501809.

[38] Y. Merroun, S. Chehab, A. El Hallaoui, R. Ghailane, S. Boukhris, and A. Souizi, “Tin Pyrophosphate (SnP2O7): As a Novel Heterogeneous and Highly Efficient Catalyst for the One Pot-Three Component Synthesis of Tetrahydrobenzo[b]Pyran and Dihydropyran[c]Chromene Derivatives,” *Iranian Journal of Chemistry and Chemical Engineering*, vol. 42, no. 7, pp. 2115–2130, 2023, doi: 10.30492/ijcce.2022.562958.5619.

[39] L. H. Brixner and G. Blasse, “Ultraviolet luminescence from hafnium pyrophosphate (HfP2O7),” *J Solid State Chem*, vol. 91, no. 2, pp. 390–393, Apr. 1991, doi: 10.1016/0022-4596(91)90095-Y.

[40] A. A. Kulkarni, V. A. Savekar, T. S. Bhat, and P. S. Patil, “Recent advances in metal pyrophosphates for electrochemical supercapacitors: A review,” *J Energy Storage*, vol. 52, p. 104986, Aug. 2022, doi: 10.1016/J.EST.2022.104986.

[41] L. H. Brixner and G. Blasse, “Ultraviolet luminescence from hafnium pyrophosphate (HfP2O7),” *J Solid State Chem*, vol. 91, no. 2, pp. 390–393, Apr. 1991, doi: 10.1016/0022-4596(91)90095-Y.

[42] J. Wallentin and M. T. Borgström, “Doping of semiconductor nanowires,” *J Mater Res*, vol. 26, no. 17, pp. 2142–2156, Sep. 2011, doi: 10.1557/jmr.2011.214.

[43] N. Manyala, J. F. DiTusa, G. Aeppli, and A. P. Ramirez, “Doping a semiconductor to create an unconventional metal,” *Nature*, vol. 454, no. 7207, pp. 976–980, Aug. 2008, doi: 10.1038/nature07137.

[44] S. C. Erwin, L. Zu, M. I. Haftel, A. L. Efros, T. A. Kennedy, and D. J. Norris, “Doping semiconductor nanocrystals,” *Nature*, vol. 436, no. 7047, pp. 91–94, Jul. 2005, doi: 10.1038/nature03832.

[45] K. Huet, F. Mazzamuto, T. Tabata, I. Toqué-Tresonne, and Y. Mori, “Doping of semiconductor devices by Laser Thermal Annealing,” *Mater Sci Semicond Process*, vol. 62, pp. 92–102, May 2017, doi: 10.1016/j.mssp.2016.11.008.

[46] M. Boshir Ahmed *et al.*, “General Doping Chemistry of Carbon Materials,” *ChemNanoMat*, vol. 9, no. 4, Apr. 2023, doi: 10.1002/cnma.202200482.

[47] C. Honsberg and S. Bowden, “Doping.” [Online]. Available: https://www.pveducation.org/pvcdrom/pn-junctions/doping

[48] Z. Xu *et al.*, “Co-doping strategy enhanced the ionic conductivity and excellent lithium stability of garnet-type Li7La3Zr2O12 electrolyte in all solid-state lithium batteries,” *Journal of Materiomics*, vol. 9, no. 4, pp. 651–660, Jul. 2023, doi: 10.1016/j.jmat.2023.01.007.

[49] Y. Li, T. Kunitake, Y. Aoki, and E. Muto, “Efficient, anhydrous proton-conducting nanofilms of Y-doped zirconium pyrophosphate at intermediate temperatures,” *Advanced Materials*, vol. 20, no. 12, pp. 2398–2404, Jun. 2008, doi: 10.1002/adma.200702590.

[50] Y. Jin, Y. Shen, and T. Hibino, “Proton conduction in metal pyrophosphates (MP2O7) at intermediate temperatures,” *J Mater Chem*, vol. 20, no. 30, pp. 6214–6217, 2010, doi: 10.1039/B924188D.

[51] T. Famprikis, P. Canepa, J. A. Dawson, M. S. Islam, and C. Masquelier, “Fundamentals of inorganic solid-state electrolytes for batteries,” *Nat Mater*, vol. 18, no. 12, pp. 1278–1291, Dec. 2019, doi: 10.1038/S41563-019-0431-3.

[52] H. Guler and F. Kurtulus, “A microwave-assisted route for the solid-state synthesis of lead pyrophosphate, Pb2P2O7,” *J Mater Sci*, vol. 40, no. 24, pp. 6565–6569, Dec. 2005, doi: 10.1007/s10853-005-1809-y.

[53] T. Windarti, Taslimah, A. Haris, Y. Astuti, and A. Darmawan, “Synthesis of β-Calcium Pyrophosphate by sol-gel method,” *IOP Conf Ser Mater Sci Eng*, vol. 172, p. 012058, Feb. 2017, doi: 10.1088/1757-899X/172/1/012058.

[54] O. Kaygili, S. Keser, T. Ates, and F. Yakuphanoglu, “Synthesis and characterization of lithium calcium phosphate ceramics,” *Ceram Int*, vol. 39, no. 7, pp. 7779–7785, Sep. 2013, doi: 10.1016/j.ceramint.2013.03.037.

[55] D. Griesiute *et al.*, “Synthesis, structural and luminescent properties of Mn-doped calcium pyrophosphate (Ca2P2O7) polymorphs,” *Sci Rep*, vol. 12, no. 1, p. 7116, May 2022, doi: 10.1038/s41598-022-11337-y.

[56] B. Singh, J.-H. Kim, J.-Y. Park, and S.-J. Song, “Ionic conductivity of Mn2+ doped dense tin pyrophosphate electrolytes synthesized by a new co-

precipitation method," *J Eur Ceram Soc*, vol. 34, no. 12, pp. 2967–2976, Oct. 2014, doi: 10.1016/j.jeurceramsoc.2014.04.024.

[57] M. S. Dahiya, V. K. Tomer, and S. Duhan, "Metal–ferrite nanocomposites for targeted drug delivery," in *Applications of Nanocomposite Materials in Drug Delivery*, Elsevier, 2018, ch. 31, pp. 737–760. doi: 10.1016/B978-0-12-813741-3.00032-7.

[58] E. D. Rodeghiero, B. C. Moore, B. S. Wolkenberg, M. Wuthenow, O. K. Tse, and E. P. Giannelis, "Sol–gel synthesis of ceramic matrix composites," *Materials Science and Engineering: A*, vol. 244, no. 1, pp. 11–21, Mar. 1998, doi: 10.1016/S0921-5093(97)00821-6.

[59] S. Kohjiya, K. Ochiai, and S. Yamashita, "Preparation of inorganic/organic hybrid gels by the sol-gel process," *J Non Cryst Solids*, vol. 119, no. 2, pp. 132–135, Apr. 1990, doi: 10.1016/0022-3093(90)90836-B.

[60] N. B. Jackson, S. G. Thoma, S. Kohler, and T. M. Nenoff, "Zirconium-Titanium Phosphate Acid Catalysts Synthesized by Sol Gel Techniques," 1998, pp. 643–649. doi: 10.1016/S0167-2991(98)80231-0.

[61] C. Hakim, N. Sabi, and I. Saadoune, "Mixed structures as a new strategy to develop outstanding oxides-based cathode materials for sodium ion batteries: A review," *Journal of Energy Chemistry*, vol. 61, pp. 47–60, Oct. 2021, doi: 10.1016/j.jechem.2021.02.027.

[62] B. Senthilkumar, Z. Khan, S. Park, K. Kim, H. Ko, and Y. Kim, "Highly porous graphitic carbon and $Ni_2P_2O_7$ for a high performance aqueous hybrid supercapacitor," *J Mater Chem A Mater*, vol. 3, no. 43, pp. 21553–21561, 2015, doi: 10.1039/C5TA04737D.

[63] P. Barpanda, S. Nishimura, and A. Yamada, "High-voltage pyrophosphate cathodes," *Adv Energy Mater*, vol. 2, no. 7, pp. 841–859, 2012.

[64] H. Wang, K. Huang, Y. Zeng, S. Yang, and L. Chen, "Electrochemical properties of TiP2O7 and LiTi2 (PO4) 3 as anode material for lithium ion battery with aqueous solution electrolyte," *Electrochim Acta*, vol. 52, no. 9, pp. 3280–3285, 2007.

[65] R. S. Borges *et al.*, "Supercapacitor operating at 200 degrees celsius," *Sci Rep*, vol. 3, no. 1, p. 2572, 2013.

[66] Q. Li, N. Mahmood, J. Zhu, Y. Hou, and S. Sun, “Graphene and its composites with nanoparticles for electrochemical energy applications,” *Nano Today*, vol. 9, no. 5, pp. 668–683, 2014.

[67] G. H. C. Prado and I. M. Prado, “Hydrogels Based on Natural Polysaccharides and Their Applications,” 2021.

[68] S. Najib and E. Erdem, “Current progress achieved in novel materials for supercapacitor electrodes: mini review,” *Nanoscale Adv*, vol. 1, no. 8, pp. 2817–2827, 2019.

[69] P. Kassanos, B. G. Rosa, M. Keshavarz, and G.-Z. Yang, “Power and data communication in wearable and implantable devices,” in *Wearable Sensors*, Elsevier, 2021, pp. 279–309.

[70] M. Sarno, “Nanotechnology in energy storage: The supercapacitors,” in *Studies in surface science and catalysis*, vol. 179, Elsevier, 2020, pp. 431–458. doi: 10.1016/B978-0-444-64337-7.00022-7.

[71] M. Goswami *et al.*, “Hybrid energy storage devices: Li-ion and Na-ion capacitors,” in *Emerging Trends in Energy Storage Systems and Industrial Applications*, Elsevier, 2023, ch. 8, pp. 223–258. doi: 10.1016/B978-0-323-90521-3.00016-8.

[72] Y. Wu, *Metal oxides in energy technologies*. Elsevier, 2018. doi: 10.1016/C2015-0-06082-8.

[73] J. Wang *et al.*, “Pseudocapacitive materials for electrochemical capacitors: from rational synthesis to capacitance optimization,” *Natl Sci Rev*, vol. 4, no. 1, pp. 71–90, Jan. 2017, doi: 10.1093/nsr/nww072.

[74] R. Yi, S. Chen, J. Song, M. L. Gordin, A. Manivannan, and D. Wang, “High-performance hybrid supercapacitor enabled by a high-rate Si-based anode,” *Adv Funct Mater*, vol. 24, no. 47, pp. 7433–7439, 2014.

[75] L. Goswami, A. Kushwaha, S. Goswami, Y. C. Sharma, T. Kim, and K. M. Tripathi, “Nanocarbon-based-ZnO nanocomposites for supercapacitor application,” in *Nanostructured Zinc Oxide*, Elsevier, 2021, pp. 553–573. doi: 10.1016/B978-0-12-818900-9.00008-5.

[76] H. Wu, H. Han, Z. Yan, Q. Zhao, and J. Chen, “Chloride solid-state electrolytes for all-solid-state lithium batteries,” *Journal of Solid State*

Electrochemistry, vol. 26, no. 9, pp. 1791–1808, 2022, doi: 10.1007/s10008-022-05230-x.

[77] S. Alipoori, S. Mazinani, S. H. Aboutalebi, and F. Sharif, "Review of PVA-based gel polymer electrolytes in flexible solid-state supercapacitors: Opportunities and challenges," *J Energy Storage*, vol. 27, p. 101072, 2020, doi: 10.1016/j.est.2019.101072.

[78] Ö. U. Kudu *et al.*, "A review of structural properties and synthesis methods of solid electrolyte materials in the Li2S− P2S5 binary system," *J Power Sources*, vol. 407, pp. 31–43, 2018, doi: 10.1016/j.jpowsour.2018.10.037.

[79] L. Yu and G. Z. Chen, "Ionic liquid-based electrolytes for supercapacitor and supercapattery," *Front Chem*, vol. 7, p. 272, 2019.

[80] A. Boudghene Stambouli and E. Traversa, "Fuel cells, an alternative to standard sources of energy," *Renewable and Sustainable Energy Reviews*, vol. 6, no. 3, pp. 295–304, 2002, doi: https://doi.org/10.1016/S1364-0321(01)00015-6.

[81] B. Sundén, "Fuel cell systems and applications," in *Hydrogen, Batteries and Fuel Cells*, Elsevier, 2019, ch. 11.3, pp. 203–216. doi: 10.1016/B978-0-12-816950-6.00011-7.

[82] T. Kulkarni and G. Slaughter, "Enzymatic Glucose Biofuel Cell and its Application," *Journal of Biochips & Tissue chips*, vol. Volume 5, p. 1000111, Jan. 2015, doi: 10.4172/21530777.1000111.

[83] A. L. Dicks and D. A. J. Rand, *Fuel cell systems explained*. John Wiley & Sons, 2018.

[84] Doitpoms.ac.uk, "Types of fuel cells." Accessed: Jan. 15, 2024. [Online]. Available: https://www.doitpoms.ac.uk/tlplib/fuel-cells/types.php

[85] L. Wang, B. Chen, J. Ma, G. Cui, and L. Chen, "Reviving lithium cobalt oxide-based lithium secondary batteries-toward a higher energy density," *Chem Soc Rev*, vol. 47, no. 17, pp. 6505–6602, 2018, doi: 10.1039/C8CS00322J.

[86] V. Srinivasan and J. Newman, "Discharge Model for the Lithium Iron-Phosphate Electrode," *J Electrochem Soc*, vol. 151, no. 10, p. A1517, 2004, doi: 10.1149/1.1785012.

[87] J. Wang, X. He, E. Paillard, N. Laszczynski, J. Li, and S. Passerini, "Lithium- and Manganese-Rich Oxide Cathode Materials for High-Energy Lithium Ion Batteries," *Adv Energy Mater*, vol. 6, no. 21, Nov. 2016, doi: 10.1002/aenm.201600906.

[88] H. Karami, M. A. Karimi, S. Haghdar, A. Sadeghi, R. Mir-Ghasemi, and S. Mahdi-Khani, "Synthesis of lead oxide nanoparticles by Sonochemical method and its application as cathode and anode of lead-acid batteries," *Mater Chem Phys*, vol. 108, no. 2–3, pp. 337–344, Apr. 2008, doi: 10.1016/j.matchemphys.2007.09.045.

[89] A. Casimir, H. Zhang, O. Ogoke, J. C. Amine, J. Lu, and G. Wu, "Silicon-based anodes for lithium-ion batteries: Effectiveness of materials synthesis and electrode preparation," *Nano Energy*, vol. 27, pp. 359–376, Sep. 2016, doi: 10.1016/j.nanoen.2016.07.023.

[90] Q. Zhang, S. Liu, Y. Lu, L. Xing, and W. Li, "Artificial interphases enable dendrite-free Li-metal anodes," *Journal of Energy Chemistry*, vol. 58, pp. 198–206, Jul. 2021, doi: 10.1016/j.jechem.2020.09.030.

[91] G. E. Blomgren, "Liquid electrolytes for lithium and lithium-ion batteries," *J Power Sources*, vol. 119–121, pp. 326–329, Jun. 2003, doi: 10.1016/S0378-7753(03)00147-2.

[92] Y. N. Sudhakar, M. Selvakumar, and D. K. Bhat, "Biopolymer Electrolytes for Fuel Cell Applications," in *Biopolymer Electrolytes*, Elsevier, 2018, pp. 151–166. doi: 10.1016/B978-0-12-813447-4.00005-4.

[93] X. Ge, F. Zhang, L. Wu, Z. Yang, and T. Xu, "Current Challenges and Perspectives of Polymer Electrolyte Membranes," *Macromolecules*, vol. 55, no. 10, pp. 3773–3787, May 2022, doi: 10.1021/acs.macromol.1c02053.

[94] A. Baktash, J. C. Reid, Q. Yuan, T. Roman, and D. J. Searles, "Shaping the future of solid-state electrolytes through computational modeling," *Advanced Materials*, vol. 32, no. 18, p. 1908041, 2020, doi: 10.1002/adma.201908041.

[95] M. V Reddy, C. M. Julien, A. Mauger, and K. Zaghib, "Sulfide and oxide inorganic solid electrolytes for all-solid-state Li batteries: a review," *Nanomaterials*, vol. 10, no. 8, p. 1606, 2020, doi: 10.3390/nano10081606.

[96] S. Payandeh *et al.*, "Nido-Borate/Closo-Borate mixed-anion electrolytes for all-solid-state batteries," *Chemistry of Materials*, vol. 32, no. 3, pp. 1101–1110, 2020, doi: 10.1021/acs.chemmater.9b03933.

[97] A. Hayashi, A. Sakuda, and M. Tatsumisago, "Development of sulfide solid electrolytes and interface formation processes for bulk-type all-solid-state Li and Na batteries," *Front Energy Res*, vol. 4, p. 25, 2016.

[98] S. J. Marje, P. K. Katkar, S. S. Pujari, S. A. Khalate, A. C. Lokhande, and U. M. Patil, "Regulated micro-leaf like nickel pyrophosphate as a cathode electrode for asymmetric supercapacitor," *Synth Met*, vol. 259, p. 116224, 2020.

[99] H. Pang, Y.-Z. Zhang, Z. Run, W.-Y. Lai, and W. Huang, "Amorphous nickel pyrophosphate microstructures for high-performance flexible solid-state electrochemical energy storage devices," *Nano Energy*, vol. 17, pp. 339–347, 2015.

[100] "The Materials Project." Accessed: Mar. 14, 2023. [Online]. Available: https://next-gen.materialsproject.org/materials/mp-770092/

[101] M. A. Nanny and R. A. Minear, "Characterization of soluble unreactive phosphorus using 31P nuclear magnetic resonance spectroscopy," *Mar Geol*, vol. 139, no. 1–4, pp. 77–94, Jun. 1997, doi: 10.1016/S0025-3227(96)00098-9.

[102] B. J. Cade-Menun, M. R. Carter, D. C. James, and C. W. Liu, "Phosphorus Forms and Chemistry in the Soil Profile under Long-Term Conservation Tillage: A Phosphorus-31 Nuclear Magnetic Resonance Study," *J Environ Qual*, vol. 39, no. 5, pp. 1647–1656, Sep. 2010, doi: 10.2134/jeq2009.0491.

[103] M. P. Williamson, "Progress in Nuclear Magnetic Resonance Spectroscopy Using chemical shift perturbation to characterise ligand binding," *Prog Nucl Magn Reson Spectrosc*, vol. 73, pp. 1–16, 2013, doi: 10.1016/j.pnmrs.2013.02.001.

[104] M. Tang and D. Lam, "Paramagnetic solid-state NMR of proteins," *Solid State Nucl Magn Reson*, vol. 103, no. June, pp. 9–16, 2019, doi: 10.1016/j.ssnmr.2019.101621.

[105] P. Schanda and M. Ernst, “Studying Dynamics by Magic-Angle Spinning Solid-State NMR Spectroscopy: Principles and Applications to Biomolecules.,” *Prog Nucl Magn Reson Spectrosc*, vol. 96, pp. 1–46, Aug. 2016, doi: 10.1016/j.pnmrs.2016.02.001.

[106] I. Martin and A. V Balatsky, “Doping-induced inhomogeneity in high-Tc superconductors,” *Physica C Supercond*, vol. 357–360, pp. 46–48, 2001, doi: https://doi.org/10.1016/S0921-4534(01)00192-7.

[107] D. Navas, S. Fuentes, A. Castro-Alvarez, and E. Chavez-Angel, “Review on Sol-Gel Synthesis of Perovskite and Oxide Nanomaterials,” 2021. doi: 10.3390/gels7040275.

[108] J. C. C. Chan, *Solid State NMR*, vol. 306. Berlin, Heidelberg: Springer Berlin Heidelberg, 2012. doi: 10.1007/978-3-642-24803-0.

[109] M. J. Duer, *Solid-State NMR Spectroscopy Principles and Applications*. Wiley, 2001. doi: 10.1002/9780470999394.

[110] A. S. Borisov, P. Hazendonk, and P. G. Hayes, “Solid-State Nuclear Magnetic Resonance Spectroscopy: A Review of Modern Techniques and Applications for Inorganic Polymers,” *J Inorg Organomet Polym Mater*, vol. 20, no. 2, pp. 183–212, 2010, doi: 10.1007/s10904-010-9358-5.

[111] BRUKER, “Avance Beginners Guide - Sample Tube.” Accessed: Jul. 12, 2023. [Online]. Available: http://www2.chem.uic.edu/nmr/downloads/bruker/en-US/html/Avance Beginners Guide/en-US/18014398881662987.html

[112] X. Wang, S. Tan, X.-Q. Yang, and E. Hu, “Pair distribution function analysis: Fundamentals and application to battery materials,” *Chinese Physics B*, vol. 29, no. 2, p. 028802, Feb. 2020, doi: 10.1088/1674-1056/ab6656.

[113] Peter Larkin, *Infrared and Raman Spectroscopy: Principles and Spectral Interpretation*, 2nd ed. Elsevier, 2017. doi: 10.1016/C2015-0-00806-1.

[114] PubChem, “Hafnium pyrophosphate.” Accessed: Aug. 16, 2023. [Online]. Available: https://pubchem.ncbi.nlm.nih.gov/compound/Hafnium-pyrophosphate

[115] A. Benzaouak *et al.*, "ZrP2O7 as a Cathodic Material in Single-Chamber MFC for Bioenergy Production," *Nanomaterials*, vol. 12, p. 3330, Sep. 2022, doi: 10.3390/nano12193330.

[116] S. Seyyidoğlu, M. Özenbaş, N. Yazıcı, and A. Yılmaz, "Investigation of solid solution of ZrP2O7–Sr2P2O7," *J Mater Sci*, vol. 42, no. 15, pp. 6453–6463, Aug. 2007, doi: 10.1007/s10853-006-0673-8.

[117] A. Armigliato, "Analysis of crystal defects by transmission electron microscopy," *Materials Chemistry*, vol. 4, no. 3, pp. 453–471, Sep. 1979, doi: 10.1016/0390-6035(79)90034-8.

[118] F. Ernst, O. Kienzle, and M. Rühle, "Structure and Composition of Grain Boundaries in Ceramics," *J Eur Ceram Soc*, vol. 19, no. 6–7, pp. 665–673, Jun. 1999, doi: 10.1016/S0955-2219(98)00294-5.

[119] C. Barry Carter and David B. Williams, *Transmission Electron Microscopy: Diffraction, Imaging, and Spectrometry*. Cham: Springer International Publishing, 2016. doi: 10.1007/978-3-319-26651-0.

[120] D. J. H. Cockayne, J. R. Parsons, and C. W. Hoelke, "A study of the relationship between lattice fringes and lattice planes in electron microscope images of crystals containing defects," *Philosophical Magazine*, vol. 24, no. 187, pp. 139–153, Jul. 1971, doi: 10.1080/14786437108216429.

[121] C.-L. Chen, Y.-J. Shih, J. F. Su, K.-L. Chen, and C.-P. Huang, "Mesoporous zirconium pyrophosphate for the adsorption of fluoride from dilute aqueous solutions," *Chemical Engineering Journal*, vol. 427, p. 132034, Jan. 2022, doi: 10.1016/j.cej.2021.132034.

[122] P. G. Laye, S. B. Warrington, G. R. Heal, D. M. Price, and R. Wilson, *Principles of Thermal Analysis and Calorimetry*. The Royal Society of Chemistry, 2002. doi: 10.1039/9781847551764.

[123] C. PCB SOLUTIONS, "Differential Thermal Analysis and PCB Substrate Glass Transitions." Accessed: Mar. 02, 2024. [Online]. Available: https://resources.pcb.cadence.com/blog/2020-differential-thermal-analysis-and-pcb-substrate-glass-transitions

[124] P. Křivík, S. Vaculík, P. Bača, and J. Kazelle, “In Situ Measurement of PEIS of Lead Acid Battery Cell,” *ECS Trans*, vol. 87, no. 1, pp. 307–314, Nov. 2018, doi: 10.1149/08701.0307ecst.

[125] T. Pajkossy and R. Jurczakowski, “Electrochemical impedance spectroscopy in interfacial studies,” *Curr Opin Electrochem*, vol. 1, no. 1, pp. 53–58, Feb. 2017, doi: 10.1016/j.coelec.2017.01.006.

[126] N. Meddings *et al.*, “Application of electrochemical impedance spectroscopy to commercial Li-ion cells: A review,” *J Power Sources*, vol. 480, p. 228742, Dec. 2020, doi: 10.1016/j.jpowsour.2020.228742.

[127] H. S. Magar, R. Y. A. Hassan, and A. Mulchandani, “Electrochemical Impedance Spectroscopy (EIS): Principles, Construction, and Biosensing Applications,” *Sensors*, vol. 21, no. 19, p. 6578, Oct. 2021, doi: 10.3390/s21196578.

[128] L. Stolz, M. Gaberšček, M. Winter, and J. Kasnatscheew, “Different Efforts but Similar Insights in Battery R&D: Electrochemical Impedance Spectroscopy *vs* Galvanostatic (Constant Current) Technique,” *Chemistry of Materials*, vol. 34, no. 23, pp. 10272–10278, Dec. 2022, doi: 10.1021/acs.chemmater.2c02376.

[129] B.-A. Mei, O. Munteshari, J. Lau, B. Dunn, and L. Pilon, “Physical Interpretations of Nyquist Plots for EDLC Electrodes and Devices,” *The Journal of Physical Chemistry C*, vol. 122, no. 1, pp. 194–206, Jan. 2018, doi: 10.1021/acs.jpcc.7b10582.